Axis convergence in *C. elegans* embryos

Archit Bhatnagar[a,1], **Michael Nestler**[b,1], **Peter Groß**[a,c,1,2], **Mirna Kramar**[c,2], **Mark Leaver**[a,3], **Axel Voigt**[b,d,e,4], **and Stephan W. Grill**[a,d,e,4]

[a]Max Planck Institute of Molecular Cell Biology and Genetics, Dresden, Germany

[b]Institute of Scientific Computing, TU Dresden, Dresden, Germany
[c]Biotechnology Center, TU Dresden, Dresden, Germany

[d]Cluster of Excellence Physics of Life, TU Dresden, Dresden, Germany
[e]Center for Systems Biology Dresden, Dresden, Germany

Embryos develop in a surrounding that guides key aspects of their development. For example, the anteroposterior (AP) body axis is always aligned with the geometric long axis of the surrounding eggshell in fruit flies and worms. The mechanisms that ensure convergence of the AP axis with the long axis of the eggshell remain unresolved. We investigate axis convergence in early *C. elegans* development, where the nascent AP axis, when misaligned, actively re-aligns to converge with the long axis of the egg. Here, we identify two physical mechanisms that underlie axis convergence. First, bulk cytoplasmic flows, driven by actomyosin cortical flows, can directly reposition the AP axis. Second, active forces generated within the pseudocleavage furrow, a transient actomyosin structure similar to a contractile ring, can drive a mechanical re-orientation such that it becomes positioned perpendicular to the long axis of the egg. This in turn ensures AP axis convergence. Numerical simulations, together with experiments that either abolish the pseudocleavage furrow or change the shape of the egg, demonstrate that the pseudocleavage furrow-dependent mechanism is the key driver of axis convergence. We conclude that active force generation within the actomyosin cortical layer drives axis convergence in the early nematode.

Anteroposterior body axis | *C. elegans* | Actomyosin cortex | Active matter theory | Pseudocleavage furrow

[1]A.B, M.N and P.G contributed equally to this work. [2]Present Address: Drug Discovery Sciences, Boehringer Ingelheim Pharma GmbH & Co. KG, 88397 Biberach an der Riß, Germany. [3]Present Address: Institut Curie, Paris. [4]To whom correspondence should be addressed (E-mail): A.V. (axel.voigt@tu-dresden.de), S.W.G. (grill@mpi-cbg.de).

The development of a single-cell embryo into an adult animal features the establishment of up to three anatomical body axes – anterior-posterior, dorsal-ventral and left-right. In general, these axes are intrinsic to the embryo (Goldstein and Freeman, 1997), yet consistently orient relative to geometric cues. In the nematode worm *C. elegans*, the anterior-posterior (AP) axis coincides with the geometric long axis of the ellipsoidal egg (Goldstein and Hird, 1996). However, during the establishment of the AP axis, the two axes may not always coincide. In this case, the AP axis actively converges towards the long axis of the egg (Goldstein and Hird, 1996). In this study, we seek to understand how the ellipsoidal geometry of the *C. elegans* egg directs this convergence of the AP axis with the long axis.

The orientation of the *C. elegans* AP axis is defined by the formation of mutually exclusive domains of PAR (partitioning-defective) proteins in the actomyosin cortex in the one-cell stage embryo, in particular the anterior (consisting of anterior PAR proteins, or aPARs) and posterior (consisting of posterior PAR proteins, or pPARs) domains (Guo and Kemphues, 1995; Rose and Gönczy, 2014; Motegi and Seydoux, 2013; Hoege and Hyman, 2013; Lang and Munro, 2017). These domains form as a result of cell polarity establishment about 30 minutes after fertilization. The egg is initially unpolarised, with aPARs uniformly enriched throughout the entire cortex (Cuenca et al., 2003; Cowan and Hyman, 2004; Schonegg and Hyman, 2006). Normally, centrosomes carried by the sperm-donated male pronucleus initiate polarity establishment at the site of sperm entry (O'Connell et al., 2000; Wallenfang and Seydoux, 2000; Cowan and Hyman, 2004; De Henau et al., 2020; Klinkert et al., 2019). Polarization proceeds via guided self-organized mechanochemical feedback between the PAR network (Motegi and Seydoux, 2013) and surface stresses and flows in the actomyosin cortex (Bois et al., 2011; Gross et al., 2017; Nitschke et al., 2019; Nestler and Voigt, 2022): Centrosomal microtubules load cytoplasmic pPARs onto the cortex (Wallenfang and Seydoux, 2000; Cowan and Hyman, 2004; Gross et al., 2019). Posterior PARs exclude myosin from the cortex, establishing myosin-poor domains (Motegi and Seydoux, 2013; Hoege and Hyman, 2013; Lang and Munro, 2017; Gross et al., 2019); the myosin imbalance between the pPAR domains and aPAR-rich regions generate active tension imbalances within the actomyosin cortex which drive cortical flow (Mayer et al., 2010; Bois et al., 2011). Cortical flows circulate away from the male pronucleus and towards the future anterior end (Motegi and Seydoux, 2013; Hoege and Hyman, 2013; Lang and Munro, 2017; Mayer et al., 2010), further redistributing PAR proteins by advective transport (Munro et al., 2004; Goehring et al., 2011; Mayer et al., 2010). Altogether, mutual antagonism between pPARs and aPARs and their transport by cortical flows leads to the formation of mutually exclusive domains of aPARs and pPARs: aPARs at the anterior and pPARs at the posterior (Gross et al., 2019); giving rise to a polarized cell and defining the embryonic AP body axis (Goldstein and Hird, 1996).

The ellipsoidal-like geometry of the *C. elegans* zygote is imposed by the eggshell surrounding the zygote, which forms shortly after fertilization (Johnston and Dennis, 2012). The zygote has one long axis about 50 µm in length, and two short axes about 30 µm in length (Begasse and Hyman, 2011; Riddle et al., 1997). How then is the AP axis oriented along the geometric long axis of the egg? As described above, the location of sperm entry imparts positional information to the cell polarity machinery. The sperm tends to enter the oocyte at the tip (Goldstein and Hird, 1996; Bienkowska and Cowan, 2012), possibly due to how the oocyte enters the spermatheca (Ward and Carrel, 1979; McCarter et al., 1999). In this case, the orientation of AP axis is along the long axis of the egg ellipsoid. However, occasionally the sperm enters away from the tip, yet the AP axis eventually converges with the geometric long axis (Goldstein and Hird, 1996). In these cases, the male pronucleus 'posteriorizes'; that is, it moves toward the closest tip of the embryo (Kimura and Kimura, 2020; Goldstein and Hird, 1996). This dynamically reorients the AP axis towards the long axis of the embryo, until the two axes converge. However, the physical mechanisms that drive this process of axis alignment remain poorly understood.

How does the AP axis converge towards the long axis? Cytoplasmic flows in the embryo have previously been proposed to drive posteriorization (Goldstein and Hird, 1996; Bienkowska and Cowan, 2012), and thus AP axis alignment. These flows are created by anterior-directed cortical flows at the surface (Niwayama et al., 2011). Cytoplasmic flows, in turn, could transport the male pronucleus (Kimura and Kimura, 2020; Mittasch et al., 2018) towards the closest tip. We refer to this scenario as the cytoplasmic flow-dependent mechanism. Another possibility is that cortical flows drive axis convergence in *C. elegans* embryos via the pseudocleavage furrow (Nigon et al., 1960), a contractile ring-like structure that forms at the boundary between the aPAR and pPAR domains (Cuenca et al., 2003; Cowan and Hyman, 2004). The ring arises by compressive flow-driven alignment of actin filaments (Reymann et al., 2016). The pseudocleavage furrow is dispensable for establishing the AP axis (Rose et al., 1995), but might modulate the dynamics of AP axis formation (Aras et al., 2018). In particular, if the furrow does not lie in a plane orthogonal to the long axis of the egg, constriction of the furrow (Reymann et al., 2016) would reposition it to minimise its circumference, reorienting the furrow to be in a plane orthogonal to the long axis. We refer to this scenario as the pseudocleavage furrow-dependent mechanism.

To evaluate these two mechanisms, we measure cortical flows and quantify axis convergence during AP axis establishment. We develop a mathematical model of axis convergence that recapitulates the measured flows—both cortical and cytoplasmic. An experimental reduction of cortical flows demonstrate that they are required for axis convergence. Experiments and numerical simulations that diminish the pseudocleavage furrow demonstrate that the pseudocleavage furrow-dependent mechanism is the primary driver of axis convergence, but the cytoplasmic flow-dependent mechanism also contributes. Experiments and numerical simulations that change the shape of embryos demonstrate the contribution of geometry to the rate of axis convergence: rounder embryos exhibit slower axis convergence. This reduction in rate is consistent between numerical simulations and experimental observations. This effect can also be described by a minimal model focusing on the action of the pseudocleavage furrow. Taken together, our results demonstrate how actomyosin-dependent active surface mechanics and flows translate the ellipsoidal geometry of the embryo into the orientation of the AP axis.

Results

Cortical flows drive AP axis convergence

We first set out to understand how the AP axis converges with the long axis of the embryo. To this end we observed the behaviour of PAR domains during AP axis establishment, via time-lapse imaging of the one-cell *C. elegans* embryo during this phase. We used a *C. elegans* line expressing PAR-6::mCherry (marking the anterior PAR domain) together with PAR-2::GFP (marking the posterior PAR domain) to visualise the PAR domains (see SI: Table 1). In agreement with previous observations (Goldstein and Hird, 1996), we found that in 33 out of 57 embryos where the AP axis is established off-axis (with a measured AP axis that started more than 10 deg out of convergence with the geometric long axis), the PAR domains moved such that within 7 minutes the AP axis converged with the long axis of the embryo (Figure 1a). We also find that AP axis convergence occurs concomitantly with the posteriorization of the male pronucleus (Figure 1b,c, male pronucleus visualised as a dark circle in the cytoplasm, see SI: Figure 1).

Furthermore, the angular velocity of the male pronucleus is highest when the angular position of the male pronucleus is largest; that is, the further the male pronucleus is from the posterior tip, the faster it moves toward the tip. Here, angular position refers to the angle between the long axis of the embryo and the line connecting the center of the male pronucleus to the center of the embryo. Specifically, we measured mean angular velocities of -2.1 ± 8.3 deg/s for angles between 0–10 deg compared to -18.9 ± 12.9 deg/s for angular positions between 30–40 deg (Figure 1c, negative velocities denote movements towards the posterior tip). Thus, for the range of angular positions measured (below approximately 45 deg), the rate of axis convergence is greatest when the axis is furthest displaced from the long axis.

Given the importance of cortical flows for AP axis establishment (Munro et al., 2004; Gross et al., 2019; Goehring et al., 2011), we next investigate their role in axis convergence. We used RNAi to impair function of *mlc-4*, an activator of myosin activity that regulates cortical flows (Shelton et al., 1999). In *mlc-4* RNAi embryos (Figure 1d, SI: Figure 1 b), flows were indeed reduced (see SI: Figure 3, SI: Figure 4 b,c, SI: Figure 5 b,c for comparison), the rate of axis convergence greatly diminished, and the AP axis failed to converge to the long axis (Figure 1d). Specifically, we measured mean angular velocities of -0.02 ± 0.04 deg/s for angular positions between 0–10 deg, -0.01 ± 0.03 deg/s for angular positions between 30–40 deg, with 10/18 embryos failing to re-orient their PAR domains (Figure 1e,f). Because MLC-4 activates myosin, and myosin is required for cortical flows (Shelton et al., 1999), a straightforward interpretation is that cortical flows are required for AP axis convergence (Zonies et al., 2010; Motegi et al., 2011; Tse et al., 2012).

A mathematical model accounts for AP axis convergence

To understand how cortical flows could drive axis convergence, we developed a mathematical model. The model considers both active surface flows in the cortex itself (Mayer et al., 2010) and bulk cytoplasmic flows that are a consequence of cortical flows (Niwayama et al., 2011) (see Figure 2 and SI: section 2). This mathematical model should allow us to answer two questions: 1) Do both mechanisms, the cytoplasmic flow dependent mechanism and the pseudocleavage furrow-dependent mechanism (Figure 2a), contribute to axis convergence and, if so, to what extent? 2) Are the two mechanisms together sufficient to capture the spatiotemporal dynamics of the entire process?

In the mathematical model (see SI: section 2), we approximate the geometry of the *C. elegans* embryo by a fixed ellipsoidal shape. The cortex at the surface of the ellipsoid is described in the general framework of active matter theory (Prost et al., 2015; Salbreux et al., 2012; Kruse et al., 2004) as an active nematic fluid layer (Kruse et al., 2005; Salbreux et al., 2009; Jülicher et al., 2018; Nestler and Voigt, 2022; Salbreux et al., 2022). Active stresses in this surface fluid layer arise through myosin activity (Mayer et al., 2010; Gross et al., 2019; Salbreux et al., 2012) and generate cortical flows. The cytoplasm itself is considered as an incompressible Newtonian fluid, with flows in it approximated as Stokes flow. At the interface between the cortex and the cytoplasm, the cytoplasm flows at the same velocity as the cortex; that is, cortical flows at the surface set a no-slip boundary condition for the bulk cytoplasm within the ellipsoid (Niwayama et al., 2011). The effect of bulk flows onto the surface fluid is captured by an effective frictional coefficient γ in the surface fluid layer (Mayer et al., 2010; Salbreux et al., 2012) (see SI: Equation 14). We assume that the friction between the embryo and the eggshell is negligible, and therefore consider only one friction term. With this coupling of surface and bulk flows, the cytoplasmic flow-field in the bulk is fully determined by the cortical flow-field on the surface (Niwayama et al., 2011) (see SI: Equation 15). The model considers the male pronucleus to be the organizer of active surface flows. The pronucleus is advected by the bulk cytoplasmic flows as a fluid particle with a large viscosity (Tanaka and Araki, 2000) (see SI: subsubsection 2.1.2). In addition, the male pronucleus is both in direct physical contact with the cortical layer and also attached to it via microtubules that radiate from the two centrosomes, which are

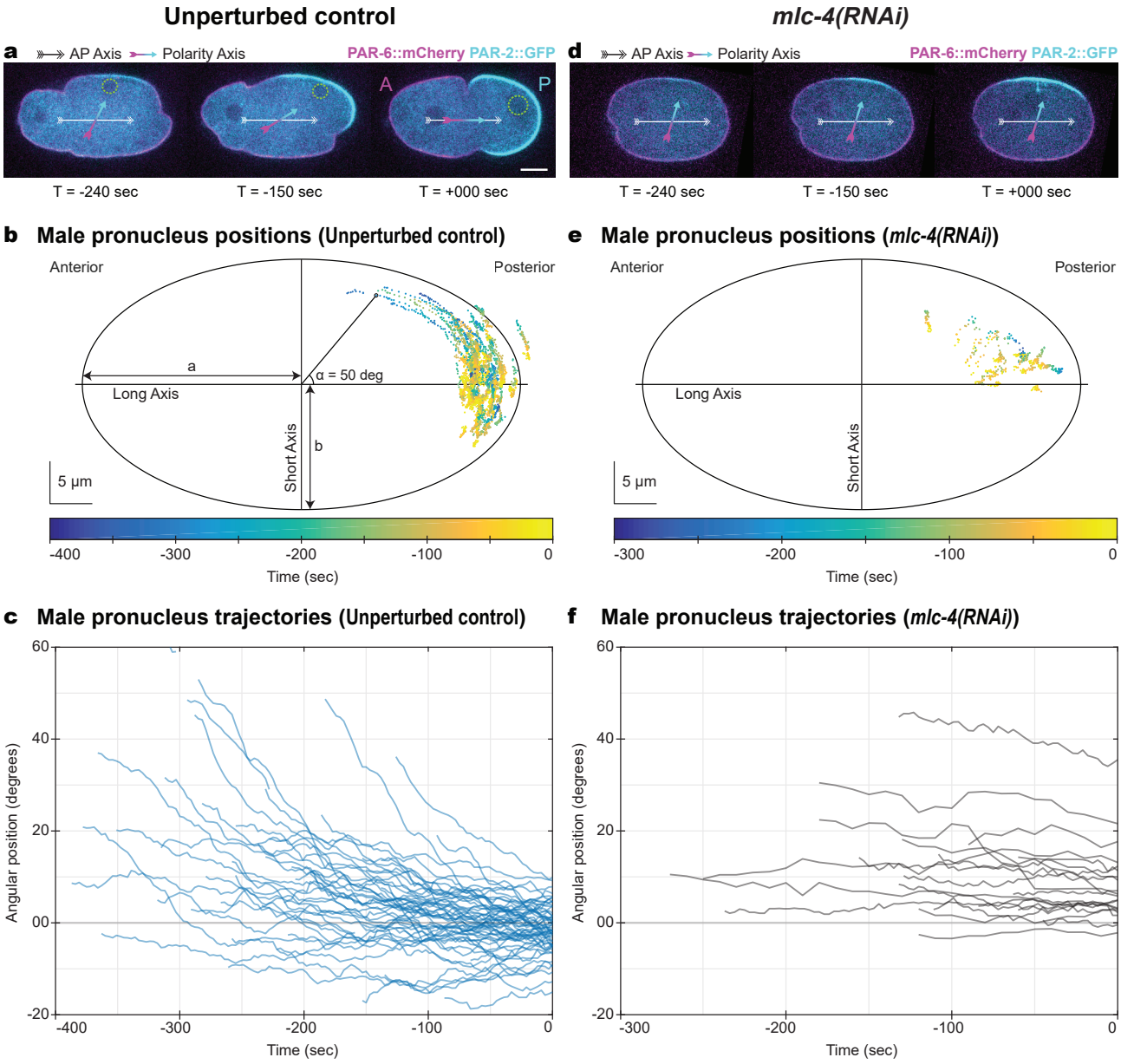

Figure 1. AP axis convergence and male pronucleus posteriorization depends on myosin activity
a) AP axis convergence in unperturbed control embryos is visualized by labeling anterior PAR (PAR-6::mCherry, in magenta) and posterior PAR (PAR-2::GFP, in cyan) domain. The male pronucleus (green dashed circle) moves with the posterior PAR domain, aligning the AP axis (cyan to magenta arrow) to the geometric long axis (White arrow). $T = 0$ s is set at the end of posteriorization. Scale bar: 10 µm (for a,d). b) Male pronucleus positions (each point represents the center) during posteriorization in NMY-2::GFP labelled (Figure 1a) unperturbed embryos, color coded by time relative to end of posteriorization (see colorbar). Scale bar: 5 µm, Ellipse has semi-major axis $a = 28.4$ µm and semi-minor axis $b = 17.5$ µm lengths (for b,e). c) Angular position of the male pronucleus (on y-axis) as a function of time relative to end of posteriorization (on x-axis), in NMY-2::GFP labelled (Figure 1a) unperturbed embryos. Each line represents an individual embryo. d) No AP axis convergence is observed in *mlc-4* RNAi embryos, noted by no re-orientation of the posterior (cyan) and anterior (magneta) PAR domains. See (a) for details. e) Male pronucleus positions in *mlc-4* RNAi embryos labelled with NMY-2::GFP (Figure 1b) or PAR-6::mCherry and PAR-2::GFP, indicating lack of posteriorization in *mlc-4* RNAi embryos. See (b) for details. f) Angular position of the male pronucleus (on y-axis) as a function of time relative to end of posteriorization (on x-axis), in *mlc-4* RNAi embryos labelled with NMY-2::GFP (Figure 1b) or PAR-6::mCherry and PAR-2::GFP. Each line represents an individual embryo.

adjacent to the male pronucleus, towards the cell cortex (Wallenfang and Seydoux, 2000; Kimura and Kimura, 2020; Bienkowska and Cowan, 2012). We capture the impact of these interactions by a drag coefficient between the male pronucleus and the cortical layer (d, see SI: Equation 18 and SI: subsubsection 2.1.2). The position of the male pronucleus determines the instantaneous distribution of myosin in the cortex and also defines the instantaneous AP axis (see SI: section 2, SI: Equation 9). The resulting gradients of myosin are responsible for the active stress distribution in the cortical layer which in turn drive cortical flows on the surface. The resulting cytoplasmic flows and its effect on the male pronucleus captures the cytoplasmic flow dependent

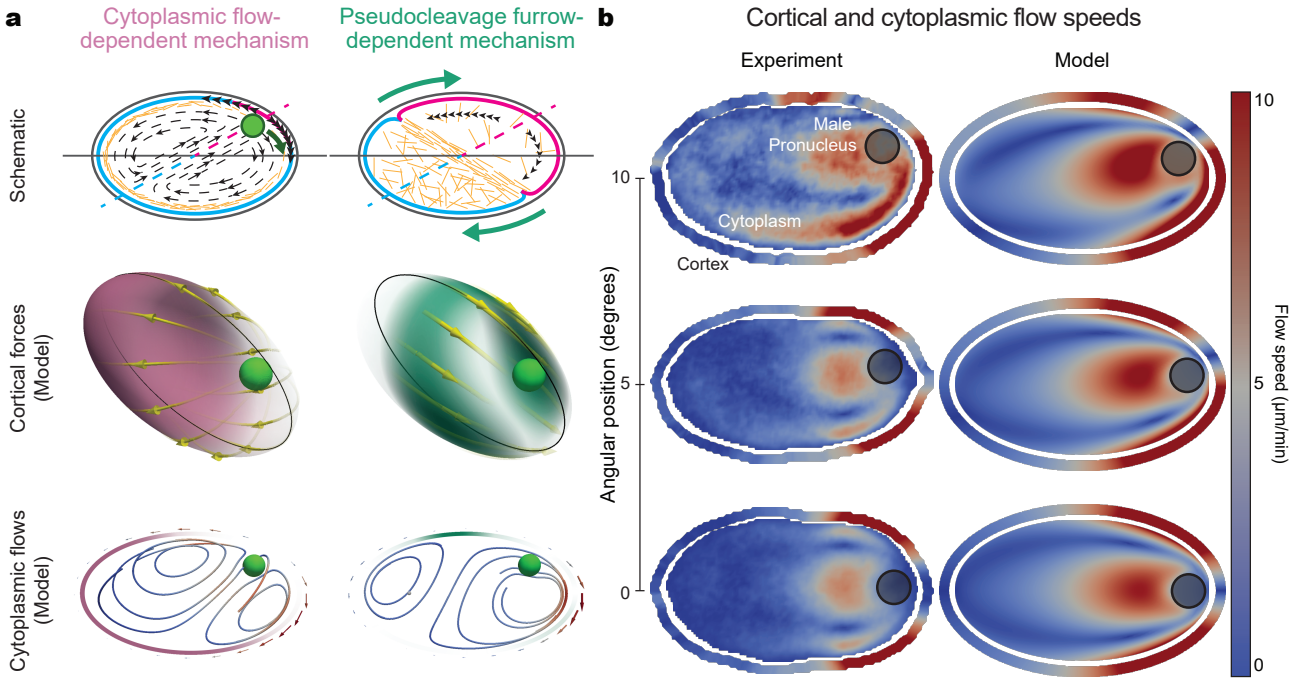

Figure 2. Numerical simulations capture the experimentally observed cortical and cytoplasmic flows during AP axis establishment in unperturbed embryos
a) Schematic detailing the two proposed mechanisms - cytoplasmic flow-dependent mechanism (left) and pseudocleavage furrow-dependent mechanism (right). 3D schematic depict the cortical forces induced by off-axis location of male pronucleus (green filled sphere) in the cortex: color represents magnitude (Transparent to red, increasing magnitude), green arrows represent direction. Black line indicates the 2D schematic boundary. In the 2D schematic, green circle represents the male pronucleus, outline around the embryo represents the cortex (transparent to red - increasing force magnitude), with black arrows representing cortical flow fields (magnitude - length of arrow). Streamlines inside the embryo represent cytoplasmic flows (blue to red - increasing speed). Each schematic represents the forces and flows that result from the corresponding mechanism alone - the full description considers both together, combined linearly. b) Cortical and cytoplasmic flow speeds, experimentally observed (left) compared to numerical simulations (right), for different male pronucleus positions (dashed green circle) in unperturbed embryos. Numerical simulations consider both cytoplasmic flow-dependent mechanism and pseudocleavage furrow-dependent mechanisms - see SI: Table 3, and SI: Figure 6. In each panel, ellipse interior represents cytoplasmic flows, and outer ellipse represents cortical flows. See colorbar for cortical flow velocities.

mechanisms of axis convergence. The pseudocleavage furrow-dependent mechanism arises due to flow-induced local shear in the cortical layer, which causes actin filaments to align (Reymann et al., 2016). Active stresses depend on the state of filament alignment. Aligned active stresses generate the pseudocleavage furrow and drive rotation of the whole cell surface (Reymann et al., 2016; Miyazaki et al., 2015) (see Figure 2a and SI: section 2, SI: Equation 12). Thus the effects of actin alignment are embodied in the pseudocleavage furrow-dependent mechanism. Consequently, the distinction between the two mechanisms is whether they take actin alignment into account (Figure 2a). Altogether, for a given position of the male pronucleus, the mathematical model calculates cortical flows, cytoplasmic flows, and flow-derived male pronucleus velocity.

We implemented the model using the adaptive finite element toolbox AMDiS (Vey and Voigt, 2007; Witkowski et al., 2015). We solved for cortical flows on the ellipsoid surface using a surface finite element method for tangential vector- and tensor-quantities (Nestler et al., 2019). We solved the Stokes problem for cytoplasmic flows in the bulk using standard finite element methods within a diffuse domain (Li et al., 2009). We solved the coupled surface (cortex) and bulk (cytoplasm) flows concurrently. We selected numerical parameters such that the numerical solutions are stable and independent of these choices (see SI: subsection 2.2 and SI: subsection 2.3). Thus, the calculation of cortical flows, cytoplasmic flows, and flow-derived pronucleus velocity depends only on the four model parameters: hydrodynamic length λ_H, active force relaxation λ_A, nematic stress relaxation λ_N and drag coefficient between the cortex and male pronucleus d (see SI: Equation 22, SI: Table 3, SI: subsubsection 2.1.2), together with the two axes lengths that describe the geometry of the egg: semi-major axis a and semi-minor axis b.

We sought model parameters that recapitulate the cortical and cytoplasmic flows we observed experimentally in unperturbed embryos. For this we set the axes of the embryo ellipsoid to match the average axes lengths (with semi-major axis length $a = 28.4\,\mu\text{m}$ and semi-minor axis length $b = 16.4\,\mu\text{m}$, SI: Figure 11 a). Because cortical flows are the basis for cytoplasmic flows, we sought parameters that result in calculated cortical flows

that best match the experimental cortical flows (see SI: subsection 2.2). Cortical flows arise from myosin depletion near the male pronucleus; based on previous work (Gross et al., 2019) the model depletes myosin within 15.9 µm of the male pronucleus. With the ellipsoid dimensions and depletion distance set, we numerically solved the model for cortical flows over a range of angular positions of the male pronucleus (0 deg to 19 deg; SI: Figure 6). Our calculated cortical flows best match our experimentally measured cortical flows with the following parameter values: hydrodynamic length $\lambda_H = 10\,\mu\text{m}$, active force relaxation $\lambda_A = 11.5\,\mu\text{m}^2\,\text{s}^{-1}$ and nematic stress relaxation $\lambda_N = 152.5\,\mu\text{m}^2\,\text{s}^{-1}$ (SI: Table 3, see SI: subsection 2.2 for calibration details). Bulk cytoplasmic flows are determined uniquely from cortical flows via the no-slip boundary condition. Calculated cytoplasmic flows show good agreement with experimental cytoplasmic flows (Figure 2b). Thus, for an optimal set of model parameters, our model faithfully recapitulates experimental cortical and cytoplasmic flows observed in unperturbed embryos.

Given that the mathematical model captures surface and bulk flow, we next evaluated how well the model predicts the movement of the male pronucleus towards the posterior tip. Specifically, we quantified: 1) angular position, taken as the angle between the line connecting the male pronucleus and embryo center to the long axis (Figure 3b), and 2) posteriorization velocity, taken as the component of the male pronucleus velocity tangential to the cortex, at the point on the cortex closest to the pronucleus (Figure 3c). The remaining model parameter that is needed to calculate male pronucleus dynamics is the drag coefficient d, which reflects direct interactions between the male pronucleus and the cortex (SI: subsubsection 2.1.2). Using model parameters that give the best match to experiment for cortical and cytoplasmic flows, we determined that a value of d =0.61 gives the best match to experimentally observed posteriorization velocities (for angular positions between 0–20 deg, Figure 3c). By integrating these best-match velocities, we obtain a predicted trajectory of the male pronucleus that agrees well with our experimental observations (SI: subsubsection 2.3.2, Figure 3b). Because numerical simulations closely match experimental measurements, we conclude that our model faithfully recapitulates the dynamics of the male pronucleus.

With this description in place, we are now in a position to evaluate to which degree the two mechanisms – the cytoplasmic flow-dependent mechanism and the pseudocleavage furrow-dependent mechanism – contribute to axis convergence.

The predominant mechanism of AP axis convergence depends on the pseudocleavage furrow

In the mathematical model, the cytoplasmic flow-dependent mechanism and the pseudocleavage furrow-dependent mechanism are additive; furrow formation requires cortical flows, but the flows - although influenced by the furrow - do not require the furrow. Recall that the pseudocleavage furrow-dependent mechanism embodies the overall effect of actin alignment, of which the major effect is the formation of the furrow. Regardless, because the two mechanisms are separable, the model enables us to probe the function of the pseudocleavage furrow in AP axis convergence. Specifically, we can assess the importance of the pseudocleavage furrow dependent mechanism by modulating the λ_N parameter, which controls the actin alignment dependent active stresses. We observe that reducing the λ_N parameter leads to slower posteriorization velocities, but the AP axis still converges to the long axis (see SI: Figure 6). Thus, the model predicts that the pseudocleavage furrow-dependent mechanism is essential to achieve normal rates of AP axis convergence.

To verify this prediction experimentally, we generated embryos lacking a pseudocleavage furrow, but with normal cortical flows. To generate embryos with unaltered cortical flows, but without a pseudocleavage furrow, we performed double RNAi of *nop-1* and *mel-11*. NOP-1 modulates activity of the small GTPase RHO-1, a major regulator of actomyosin in the early embryo (Tse et al., 2012). Embryos from mothers that are mutant for NOP-1 lack a pseudocleavage furrow (Rose et al., 1995). MEL-11 is a myosin phosphatase (Piekny and Mains, 2002) that suppresses the activity of myosin in the cortex (Najafabadi et al., 2022). RNAi of *nop-1* eliminates the pseudocleavage furrow in the embryo (Tse et al., 2012), but cortical flows are also reduced (SI: Figure 3, SI: Figure 4 c, SI: Figure 4 d, SI: subsection 3.1). Under double *nop-1; mel-11* RNAi conditions, every embryo that we observed lacked a pseudocleavage furrow (69/69 embryos). Cortical flow speeds in the double-RNAi embryos were also comparable to unperturbed controls (average cortical flow speed: $3.34 \pm 0.52\,\mu\text{m/min}$ in double RNAi of *nop-1* and *mel-11*, as compared to $4.12 \pm 0.59\,\mu\text{m/min}$ for unperturbed control embryos, see SI: subsection 3.1, SI: Figure 3, SI: Figure 4 c, SI: Figure 4 d). Thus, *nop-1; mel-11* RNAi experimentally generates embryos lacking a pseudocleavage furrow, but with normal cortical flows.

To evaluate the prediction of the mathematical model, we measured the rate of convergence in *nop-1; mel-11* RNAi embryos. Qualitatively, the rate was slower (compare Figure 3e,f and Figure 3b,c). We calibrated our model based on the experimentally observed cortical flows in *nop-1; mel-11* RNAi embryos. Because we see no pseudocleavage furrow in these embryos, we set $\lambda_N = 0\,\mu\text{m}^2\,\text{s}^{-1}$, thereby excluding the pseudocleavage furrow

dependent mechanism. Model parameters that yield the best match to experimental cortical flows for the $\lambda_N = 0\,\mu\text{m}^2\,\text{s}^{-1}$ condition are $\lambda_H = 11\,\mu\text{m}$, $\lambda_A = 7\,\mu\text{m}^2\,\text{s}^{-1}$ (see SI: Table 3 and SI: Figure 7) which indicates that cortical mechanics are slightly altered in this condition. We leave the drag coefficient d =0.61 unchanged, and find that the model prediction for the $\lambda_N = 0\,\mu\text{m}^2\,\text{s}^{-1}$ condition broadly matches both of the experimental readouts of AP axis convergence – posteriorization velocities and the male pronucleus trajectories – in *nop-1; mel-11* RNAi embryos (Figure 3e,f). Thus, the cytoplasmic flow-dependent mechanism accounts for the slow AP axis convergence in *nop-1; mel-11* perturbed embryos (Figure 3c,f; average posteriorization velocities, calculated over angular positions 0–20 deg: $-0.01 \pm 0.06\,\mu\text{m/s}$ in *nop-1; mel-11* RNAi compared to $-0.03 \pm 0.06\,\mu\text{m/s}$ for unperturbed embryos). We conclude that the predominant mechanism that drives AP axis convergence depends on the pseudocleavage furrow, as predicted by the mathematical model.

Embryo geometry directs the rate of AP axis convergence

Embryo geometry is a prominent feature of the model, represented by the lengths of the long and the two equal short axes of the ellipsoid, a and b respectively. We focus on the aspect ratio a/b. To investigate how AP axis convergence depends on geometry, we calculated posteriorization velocities for embryos with different aspect ratios while holding the volume constant, setting all other model parameters to the values for unperturbed embryos (SI: subsection 2.2). Embryos with smaller aspect ratios show slower posteriorization velocities (SI: Figure 12 a, Figure 5a). Thus, the mathematical model predicts that rounder embryos have a slower rate of AP axis convergence.

To verify this prediction experimentally, we used RNAi to knockdown *ima-3* to generate embryos with aspect ratios smaller than unperturbed embryos (Sönnichsen et al., 2005). IMA-3 is a member of the importin α family of nuclear transport factors (Geles and Adam, 2001; Sönnichsen et al., 2005). Reducing *ima-3* levels by RNAi results in smaller, rounder embryos (Sönnichsen et al., 2005), (average $a/b = 1.5 \pm 0.2$ for *ima-3* RNAi embryos compared to 1.8 ± 0.2 for unperturbed embryos, Figure 4a,b, SI: Figure 11 a). To obtain the model prediction for the rounder *ima-3* embryos, we used the same model parameters as the unperturbed embryos, but changed the aspect ratio of the ellipsoid to match the average *ima-3* RNAi embryos (SI: Table 3). Using the same model parameters is valid because both cortical flows and myosin concentrations in the cortex and cytoplasm are comparable between ima-3 RNAi and unperturbed embryos (see SI: subsection 3.2, SI: Figure 3, SI: Figure 4, SI: Figure 5 for cortical flows, SI: Figure 11 for myosin concentrations). The model prediction for this updated geometry matches both of the experimental readouts of AP axis convergence - male pronucleus trajectories and posteriorization velocities - in *ima-3* RNAi embryos (Figure 4c,d). Additionally, the experimentally-observed posteriorization velocities are faster in unperturbed embryos compared to *ima-3* embryos (Figure 4d; average posteriorization velocity over angular positions 0–20 deg: $-0.03 \pm 0.06\,\mu\text{m/s}$ for unperturbed compared to $-0.02 \pm 0.06\,\mu\text{m/s}$ in *ima-3* RNAi embryos). Consequently—as predicted by the model—rounder embryos have a slower rate of AP axis convergence.

Because our mathematical model demonstrates a theoretical relation between embryo geometry and the rate of AP axis convergence – the more spherical the embryo, the slower the rate (SI: Figure 12 a, Figure 5a) – we sought to experimentally evaluate this relation directly. Instead of considering the rate of AP axis convergence – measured as the posteriorization velocity – as a function of angular position for a given average aspect ratio (Figure 4d), we now consider the posteriorization velocity as a function of aspect ratio. To obtain a characteristic velocity for each aspect ratio, we take the average of posteriorization velocity over an intermediate angular positions (between 3–15 deg, see Figure 5c). Given that cortical flows and myosin concentrations are comparable between unperturbed and *ima-3* RNAi embryos (see SI: subsection 3.2, SI: Figure 3, SI: Figure 4, SI: Figure 5 for cortical flows, SI: Figure 11 b,c for myosin concentrations), we combined the two datasets, thus considering aspect ratios between $a/b = 1.1$–2.1. We find good agreement between the model predictions and our experimental measurements (Figure 5c). Thus, we conclude that indeed: the more spherical the embryo, the slower the rate of AP axis convergence.

A minimal model explains how geometry directs AP axis convergence

Why does the rate of AP axis convergence depend on embryo geometry? Our mathematical model and experimental results show that the predominant driver of AP axis convergence is the pseudocleavage furrow-dependent mechanism. In the mathematical model, the pseudocleavage furrow-dependent mechanism embodies the overall effect of actin convergence and associated active stresses, of which the major effect is the formation of the pseudocleavage furrow. In the embryo, the pseudocleavage furrow is a contractile ring. Thus, a simple, minimal model of AP axis convergence would be a contractile ring rotating on an ellipsoid. Is this minimal model sufficient to capture the relation between geometry and AP axis convergence?

In this minimal model (see SI: section 4), the ellipsoid has long axis of length $2a$ and short axis of length $2b$. The centers of the ring and the ellipsoid are coincident. The angle between the normal to the plane of the ring and the long axis of the ellipsoid is α. The sole degree of freedom in the model is α; thus changes in α encapsulate all the dynamics of the model. Changes in α are opposed by a coefficient of friction (Figure 5b, SI: Figure 12 b) In addition, we assume that the male pronucleus moves with the same angular velocity as the ring. For small angles α, we obtain the following relation between the posteriorization velocity v of the male pronucleus and α (SI: section 4, SI: Equation 30):

$$v \propto ab(1-(b/a)^2)\alpha$$

We find that to a reasonable extent, the simple effective model recapitulates both the experimentally observed and the simulated posteriorization velocities as a function of aspect ratio (Figure 5c). We conclude that this simple, minimal model captures the essence of the relation between geometry and AP axis convergence.

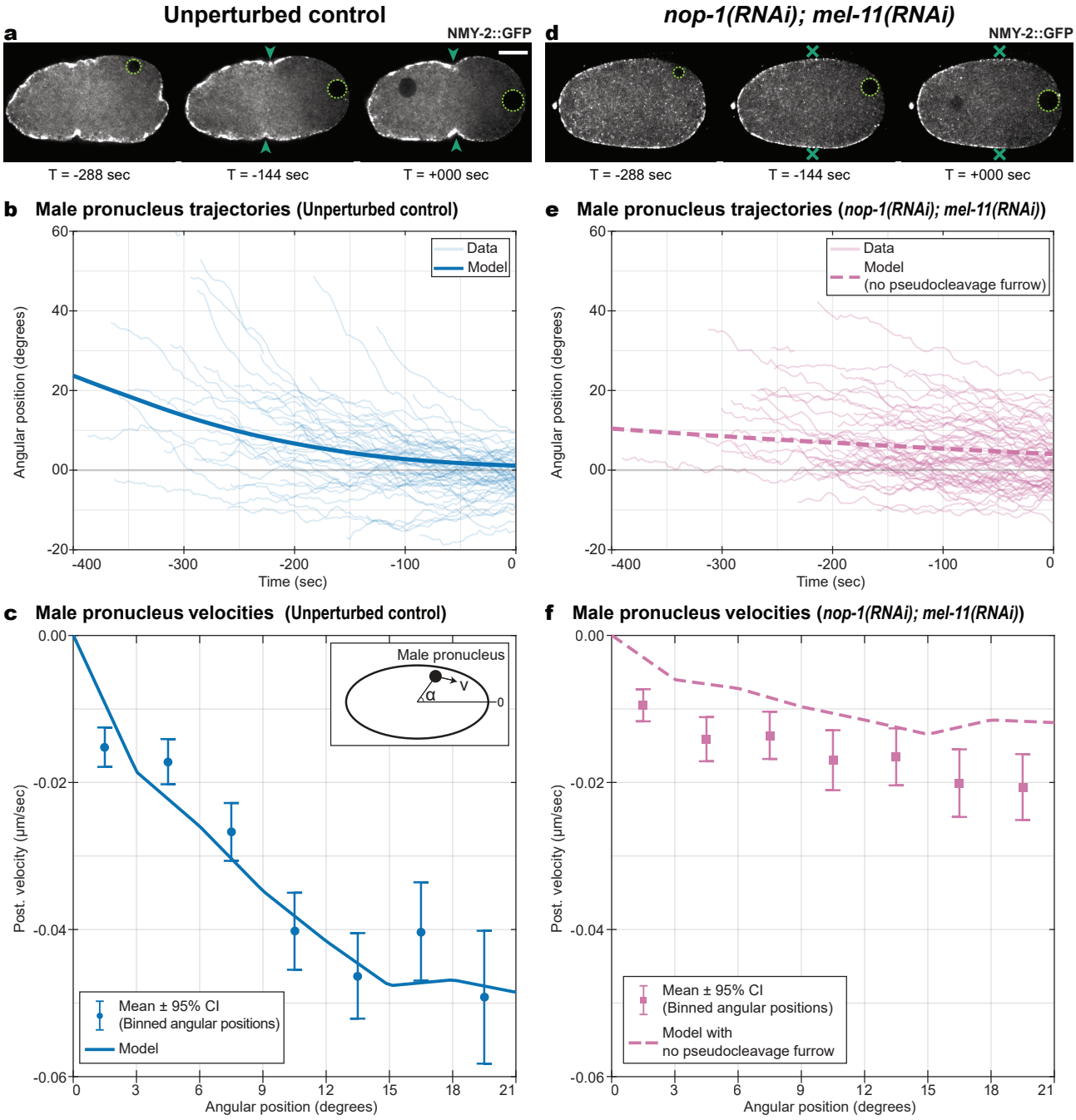

Figure 3. Experimental removal of pseudocleavage furrow via *nop-1;mel-11* RNAi reveals the role of pseudocleavage furrow in AP axis convergence

a,d) AP axis convergence observed in unperturbed control embryos (a) and *nop-1;mel-11* RNAi embryos (d) via time-lapse microscopy of embryos labelled with NMY-2::GFP (in gray). Arrows in (a) indicate the pseudocleavage furrow in unperturbed embryos, while crosses in (d) indicate the lack of the furrow in *nop-1;mel-11* RNAi embryos. $T = 0$ s denotes end of posteriorization of the male pronucleus. Scale bar: 10 µm. b,e) Angular position of the male pronucleus (on y-axis, in deg), plotted as a function of time relative to end of posteriorization (on x-axis, in s) for unperturbed control embryos ((b), N = 57 - **same data as Figure 1c**) and *nop-1;mel-11* RNAi embryos ((e), N = 69). Blue thin lines in (b) and pink thin lines in (e) represent the experimentally observed trajectories of the male pronucleus in unpertured embryos (b) and *nop-1;mel-11* RNAi embryos (e) respectively; each line is an embryo. Blue thick line in (b) represents the predicted trajectory of the male pronucleus using the full mathematical model calibrated for unperturbed embryos. Pink dashed thick line in (e) represents the predicted trajectory using the mathematical model without the pseudocleavage furrow and calibrated for *nop-1;mel-11* RNAi embryos. (see SI: subsubsection 2.3.2 and SI: subsection 2.2) c,f) Posteriorization velocity of the male pronucleus (velocity component of the male pronucleus along the cell cortex, on y-axis, in µm/s) as a function of its angular position (on x-axis, in deg) in unperturbed embryos ((c), N = 57) and in *nop-1;mel-11* RNAi embryos ((f), N = 69). See inset in (c) for visual definition. Blue circles in (c) and pink squares in (f) denote the average posteriorization velocity for each angular position bin (bin size: 3 deg), with error bars representing the 95% confidence interval of the average, measured in unperturbed embryos (c) and *nop-1;mel-11* RNAi embryos (f) respectively. Blue curve in (c) and Pink dashed curve in (f) denotes the predicted posteriorization velocities using the full mathematical model (c) and mathematical model without pseudocleavage furrow (f) respectively (see SI: subsubsection 2.3.2 and SI: subsection 2.2 for details).

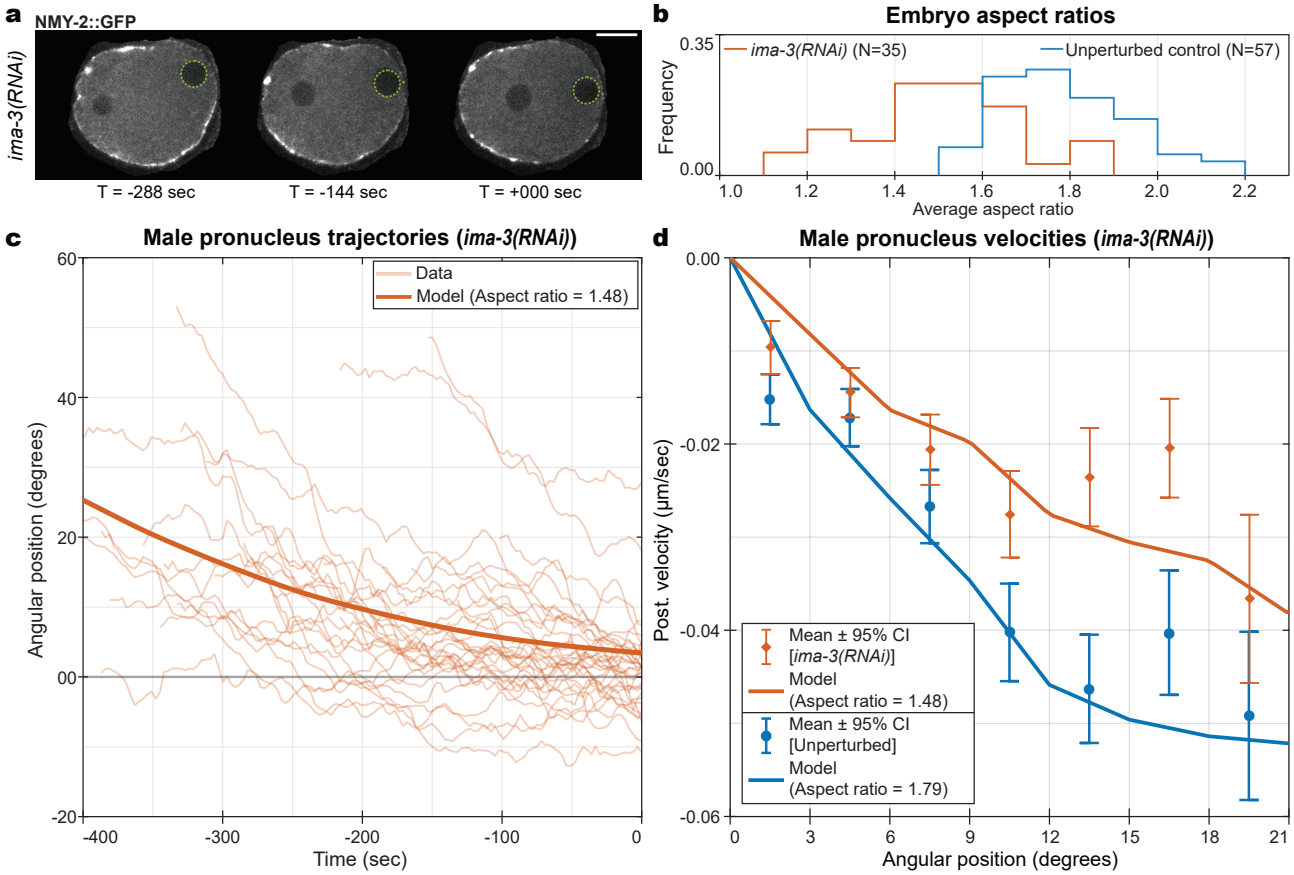

Figure 4. Rounder embryos generated by *ima-3* RNAi show slower AP axis convergence, consistent with predictions from mathematical model

a) AP axis convergence observed in rounder *ima-3* RNAi embryos via time-lapse microscopy of embryos labelled with NMY-2::GFP (in gray). $T = 0$ s denotes end of posteriorization of the male pronucleus. Scale bar: 10 µm. b) Comparing aspect ratio (Length/Width) between unperturbed and *ima-3* RNAi embryos. Histogram depicts the distribution of average aspect ratio of an embryo in unperturbed embryos (Blue, N = 57, average aspect ratio = 1.8 ± 0.2) and *ima-3* RNAi embryos (Orange, N = 35, average aspect ratio = 1.5 ± 0.2) plotted as the frequency of embryos (fraction of embryos, along y-axis) observed in a given aspect ratio bin (along x-axis, bins of width 0.1). c) Angular position of the male pronucleus (on y-axis, in deg), plotted as a function of time relative to end of posteriorization (on x-axis, in s) for *ima-3* RNAi embryos. Orange thin lines represent the experimentally observed trajectories; each line is an embryo. Orange thick line represents the predicted trajectory of the male pronucleus using the full mathematical model, using the parameters from the unperturbed embryos (SI: Table 3) for unperturbed embryos (aspect ratio: 1.48). (see SI: subsubsection 2.3.2 and SI: subsection 2.2) d) Posteriorization velocity of the male pronucleus (on y-axis, in µm/s) as a function of its angular position (on x-axis, in deg) in unperturbed embryos (blue, N = 57, reproduced from Figure 3c) and in *ima-3* RNAi embryos (orange, N = 35). See inset in Figure 3c for visual definition. Blue circles and orange diamonds denote the average posteriorization velocity for each angular position bin (bin size: 3 deg), with error bars representing the 95% confidence interval of the average, measured in unperturbed embryos (blue circles) and *ima-3* RNAi embryos (orange diamonds) respectively. Curves denote the predicted posteriorization velocities using the full mathematical model, using the parameters from the unperturbed embryos (SI: Table 3) - blue for unperturbed embryos (aspect ratio: 1.79, reproduced from Figure 3b), orange for unperturbed embryos (aspect ratio: 1.48). (see SI: subsubsection 2.3.2 and SI: subsection 2.2 for details).

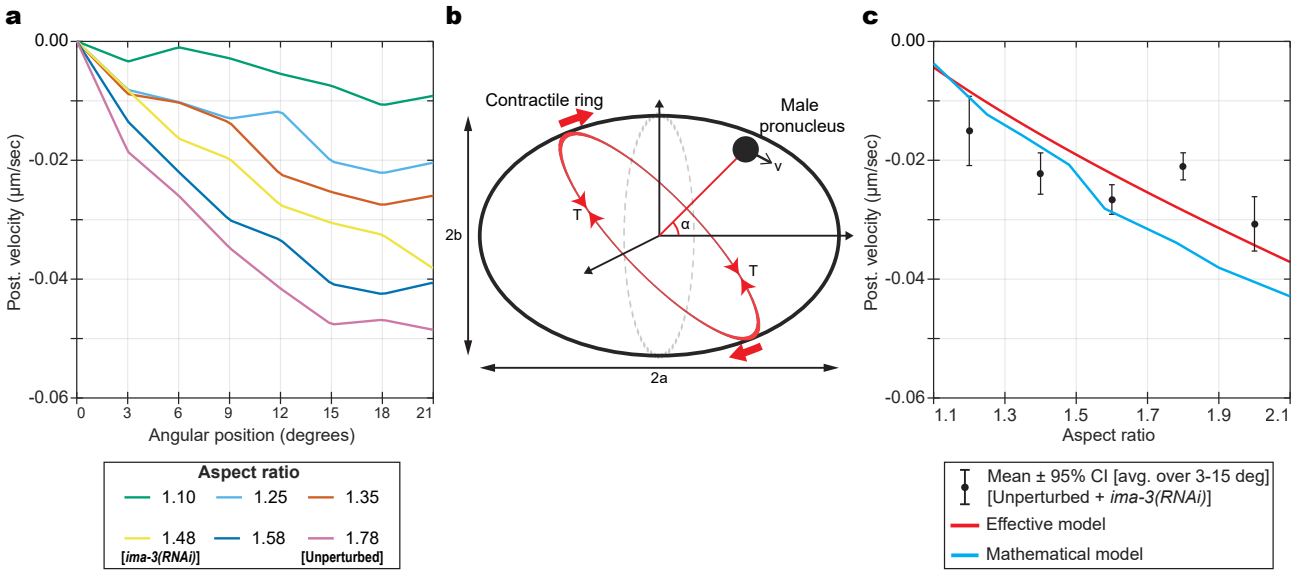

Figure 5. A minimal effective model can capture the relation between embryo geometry and rate of AP axis convergence

a) Predicted posteriorization velocity of the male pronucleus (on y-axis, in µm/s) as a function of its angular position (on x-axis, in deg) for embryo ellipsoid with different aspect ratios, using the full mathematical model. Only aspect ratio is varied, the volume of the ellipsoid is kept the same as the unperturbed embryos (SI: subsection 4.3). Aspect ratios 1.48 and 1.79 are used for predictions for *ima-3* RNAi (Figure 4d) and unperturbed embryos (Figure 3c,Figure 4d) respectively. b) Schematic depicting the effective model of a contractile ring (red ellipse) with fixed line tension (T) moving on an ellipsoid (black thick line, long axis of length $2a$ along x-axis and short axes of length $2b$ each along y- and z-axes). The ring is free to rotate around the z-axis (red block arrows). Its position is defined by the angle α between the long axis and normal to the plane of the ring, and is same as angular position of the male pronucleus. v is the posteriorization velocity of the male pronucleus. c) Posteriorization velocity of the male pronucleus (on y-axis, in µm/s) as a function of its aspect ratios (on x-axis). Black circles with error bars denote the observations from the combined unperturbed and *ima-3* RNAi embryos datasets, considering angular positions within 3–15 deg (N = 68). Black circles denote the average posteriorization velocity in each aspect ratio bin (bin size: 0.2). Error bars represent the 95% confidence interval in each bin. Curves denote the predictions from mathematical model (blue, SI: subsection 4.3) and effective model (red - $v = C(R - \frac{1}{R}), R =$ aspect ratio). For effective model, $C = -2.32 \times 10^{-2}$ µm/s (SI: section 4).

Discussion

Here, we show that in *C. elegans* two partially redundant, additive mechanisms drive the convergence of the AP axis with the geometric long axis of the egg. Both are driven by flows in the actomyosin cortex, which behaves as an active nematic fluid layer. Flows in the cortical layer are organised by the centrosomes associated with the male pronucleus (Gross et al., 2019; Wallenfang and Seydoux, 2000). Cortical flows generate cytoplasmic flows and the pseudocleavage furrow. Both features translate the geometry of the ellipsoidal embryo to orient the AP axis towards the long axis of the embryo. Typically, both mechanisms are engaged, but the pseudocleavage furrow-dependent mechanism dominates.

Previous work has shown that the pseudocleavage furrow is largely dispensable for proper AP axis formation and orientation (Rose et al., 1995; Cowan and Hyman, 2004). We argue that in embryos without a pseudocleavage furrow, AP axis convergence takes place because the cytoplasmic flows advect the male pronucleus towards the closest tip. In embryos with a pseudocleavage furrow, AP axis convergence takes place rapidly, since the male pronucleus migrates quickly due to action of the furrow. Furthermore in pseudocleavage furrow-deficient embryos, incomplete AP axis convergence early in development could be corrected later by slow movement of PAR domains (Mittasch et al., 2018; Geßele et al., 2020). Such a correction may also be geometry-dependent, due to the tendency of PAR domains to form in regions of high curvature (Klinkert et al., 2019). Thus, multiple redundant mechanisms ensure proper positioning of the AP axis even if the pseudocleavage furrow fails to form.

To conclude, the AP axis converges to the long axis because cortical flows translate the geometry of the embryo into directed movement. The cortical layer is sensitive to geometry due to the nematic nature of the cortex: the alignment of actin filaments in the cortical layer depends on local curvature. Myosin motors acting on aligned filaments generate active anisotropic stresses physically embodied as the pseudocleavage furrow (Reymann et al., 2016). The nematic ordering of actin filaments thus gives rise to curvature-sensitive stresses that leads to the rotation of the pseudocleavage furrow, a directional movement. Previous studies have explored the relation between geometry and the behaviour of nematic materials (Giomi, 2015; Nitschke et al., 2018, 2020; Maroudas-Sacks et al., 2021; Nestler and Voigt, 2022; Hoffmann et al., 2022; Bell et al., 2022; Salbreux et al., 2022; Nitschke et al., 2022). Here, our mathematical model shows how the nematic behaviours of the actomyosin cortex in the context of the ellipsoidal shape of the embryo give rise to the orientation of an anatomical feature – the AP axis of the *C. elegans* embryo.

The explanatory power of the mathematical model arises from integrating the effects of the cortex and cytoplasm, the shape of the embryo, and the reorientation of the AP axis into a coherent whole. It demonstrated the primary importance of geometry and the action of the pseudocleavage furrow in AP axis convergence. Indeed, a minimal model based only on these two features – geometry and the furrow – recapitulates the essence of AP axis convergence. Many of the features analysed here are general to many biological systems: self organizing pattern formation (PAR domains) (Goldstein and Freeman, 1997; John Gerhart, 1997), mechanical forces (cortical flows) (Sagy et al., 2019; Etoc et al., 2016; Zhang et al., 2019; Gross et al., 2017; Münster et al., 2018), anatomy (body axes) (Hiramatsu et al., 2013; Vianello and Lutolf, 2019; Mesnard et al., 2004), and physical cues in the environment (egg geometry) (Miyazaki et al., 2015; Jülicher et al., 2018; Nitschke et al., 2020; Salbreux et al., 2022; Nitschke et al., 2022). Integration of these general features into holistic models in other experimental contexts should establish general principles of the interplay between active mechanics and geometry during development.

Methods

C. elegans strains were cultured using standard culture methods (Brenner, 1974), and maintained at 20 °C. See SI: Table 1 for a list of *C. elegans* strains used in this study. RNAi interference was performed using the feeding method, see (Kamath and Ahringer, 2003). See SI: section 1 for details on RNAi experiments.

Time-lapse movies of the mid-plane cross-section of *C. elegans* embryos were obtained at room temperature. This was done using an Axio Observer Z1 - ZEISS spinning disk confocal microscope equipped with a CSU-X1 Yokogawa spinning disk head using a 63X / 1.2 NA PlanApochromat objective. PAR domains were visualized using this system equipped with an Andor iXon emCCD camera. Posteriorization of male pronucleus and cortical flows were visualized using this system equipped with a Hamamatsu ORCA-Flash4.0 V2 CMOS camera. See SI: section 1 for details on microscopy and mounting methods.

These time-lapse movies of *C. elegans* embryos were analysed to quantify the following: embryo geometry, posteriorization of the male pronucleus and cortical flows. Embryo geometry was quantified by fitting an ellipse to the boundary of the embryo mid-plane observed in the movies. Posteriorization was quantified by tracking the male pronucleus, identified as a dark circle in the cytoplasm in fluorescent microscopy images. Cortical flows were quantified similarly to (Gross et al., 2019) using particle image velocimetry on the cortical layer of the embryo, identified as a 15 pixel wide layer at the boundary of the embryo mid-plane. Only NMY-2::GFP labelled embryos were used for measuring cortical flows. See SI: section 1 for details on image analysis.

See SI: section 1 for further details on experimental methods. See SI: section 2 for details on the mathematical model and numerical simulations. See SI: section 4 for details regarding the minimal model.

Bibliography

Aras, B. S., Zhou, Y., Dawes, A., and Chou, C.-S. The importance of mechanical constraints for proper polarization and psuedo-cleavage furrow generation in the early caenorhabditis elegans embryo. *PLoS Computational Biology*, 14 (7):e1006294, 2018.

Begasse, M. L. and Hyman, A. A. *The First Cell Cycle of the Caenorhabditis elegans Embryo: Spatial and Temporal Control of an Asymmetric Cell Division*, pages 109–133. Springer Berlin Heidelberg, Berlin, Heidelberg, 2011. ISBN 978-3-642-19065-0. doi: 10.1007/978-3-642-19065-0_6. URL `https://doi.org/10.1007/978-3-642-19065-0_6`.

Bell, S., Lin, S.-Z., Rupprecht, J.-F., and Prost, J. Active nematic flows over curved surfaces. *Physical Review Letters*, 129(11):118001, 2022.

Bienkowska, D. and Cowan, C. R. Centrosomes can initiate a polarity axis from any position within one-cell c. elegans embryos. *Current Biology*, 22(7):583–589, 2012.

Bois, J. S., Jülicher, F., and Grill, S. W. Pattern formation in active fluids. *Physical Review Letters*, 106(2):028103, 2011.

Brenner, S. The genetics of caenorhabditis elegans. *Genetics*, 77(1):71–94, 1974.

Cowan, C. R. and Hyman, A. A. Asymmetric cell division in c. elegans: cortical polarity and spindle positioning. *Annu. Rev. Cell Dev. Biol.*, 20:427–453, 2004.

Cowan, C. R. and Hyman, A. A. Centrosomes direct cell polarity independently of microtubule assembly in c. elegans embryos. *Nature*, 431(7004):92–96, 2004.

Cuenca, A. A., Schetter, A., Aceto, D., Kemphues, K., and Seydoux, G. Polarization of the c. elegans zygote proceeds via distinct establishment and maintenance phases. *Development*, 2003.

De Henau, S., Pagès-Gallego, M., Pannekoek, W.-J., and Dansen, T. B. Mitochondria-derived h2o2 promotes symmetry breaking of the c. elegans zygote. *Developmental cell*, 53(3):263–271, 2020.

Etoc, F., Metzger, J., Ruzo, A., Kirst, C., Yoney, A., Ozair, M. Z., Brivanlou, A. H., and Siggia, E. D. A balance between secreted inhibitors and edge sensing controls gastruloid self-organization. *Developmental Cell*, 39(3):302–315, 2016.

Geles, K. G. and Adam, S. A. Germline and developmental roles of the nuclear transport factor importin (α) 3 in c. elegans. *Development*, 128(10):1817–1830, 2001.

Geßele, R., Halatek, J., Würthner, L., and Frey, E. Geometric cues stabilise long-axis polarisation of par protein patterns in c. elegans. *Nature Communications*, 11(1):1–12, 2020.

Giomi, L. Geometry and topology of turbulence in active nematics. *Physical Review X*, 5(3):031003, 2015.

Goehring, N. W., Trong, P. K., Bois, J. S., Chowdhury, D., Nicola, E. M., Hyman, A. A., and Grill, S. W. Polarization of par proteins by advective triggering of a pattern-forming system. *Science*, 334(6059):1137–1141, 2011.

Goldstein, B. and Freeman, G. Axis specification in animal development. *BioEssays*, 19(2):105–116, 1997. doi: https://doi.org/10.1002/bies.950190205.

Goldstein, B. and Hird, S. N. Specification of the anteroposterior axis in caenorhabditis elegans. *Development*, 122(5): 1467–1474, 1996.

Gross, P., Kumar, K. V., and Grill, S. W. How active mechanics and regulatory biochemistry combine to form patterns in development. *Annual Review of Biophysics*, 46(1):337–356, 2017. doi: 10.1146/annurev-biophys-070816-033602. PMID: 28532214.

Gross, P., Kumar, K. V., Goehring, N. W., Bois, J. S., Hoege, C., Jülicher, F., and Grill, S. W. Guiding self-organized pattern formation in cell polarity establishment. *Nature Physics*, 15(3):293–300, 2019.

Guo, S. and Kemphues, K. J. par-1, a gene required for establishing polarity in c. elegans embryos, encodes a putative ser/thr kinase that is asymmetrically distributed. *Cell*, 81(4):611–620, 1995.

Hiramatsu, R., Matsuoka, T., Kimura-Yoshida, C., Han, S.-W., Mochida, K., Adachi, T., Takayama, S., and Matsuo, I. External mechanical cues trigger the establishment of the anterior-posterior axis in early mouse embryos. *Developmental Cell*, 27(2):131–144, 2013.

Hoege, C. and Hyman, A. A. Principles of par polarity in caenorhabditis elegans embryos. *Nature Reviews Molecular Cell Biology*, 14(5):315–322, 2013.

Hoffmann, L. A., Carenza, L. N., Eckert, J., and Giomi, L. Theory of defect mediated morphogenesis. *Sci. Adv.*, 8: eabk2712, 2022.

John Gerhart, M. K. *Cells, Embryos, And Evolution*. Blackwell Science, 1997. ISBN 0-86542-574-4.

Johnston, W. and Dennis, J. The eggshell in the c. elegans oocyte-to-embryo transition. *Genesis (New York, N.Y. : 2000)*, 50:333–49, 04 2012. doi: 10.1002/dvg.20823.

Jülicher, F., Grill, S. W., and Salbreux, G. Hydrodynamic theory of active matter. *Reports on Progress in Physics*, 81 (7):076601, 2018.

Kamath, R. S. and Ahringer, J. Genome-wide rnai screening in caenorhabditis elegans. *Methods*, 30(4):313–321, 2003.

Kimura, K. and Kimura, A. Cytoplasmic streaming drifts the polarity cue and enables posteriorization of the caenorhabditis elegans zygote at the side opposite of sperm entry. *Molecular Biology of the Cell*, 31(16):1765–1773, 2020. doi: 10.1091/mbc.E20-01-0058. PMID: 32459552.

Klinkert, K., Levernier, N., Gross, P., Gentili, C., von Tobel, L., Pierron, M., Busso, C., Herrman, S., Grill, S. W., Kruse, K., et al. Aurora a depletion reveals centrosome-independent polarization mechanism in caenorhabditis elegans. *Elife*, 8:e44552, 2019.

Kruse, K., Joanny, J. F., Jülicher, F., Prost, J., and Sekimoto, K. Asters, vortices, and rotating spirals in active gels of polar filaments. *Phys. Rev. Lett.*, 92:078101, Feb 2004. doi: 10.1103/PhysRevLett.92.078101.

Kruse, K., Joanny, J. F., Jülicher, F., Prost, J., and Sekimoto, K. Generic theory of active polar gels: a paradigm for cytoskeletal dynamics. *The European Physical Journal E*, 16:5–16, 2005.

Lang, C. F. and Munro, E. The par proteins: from molecular circuits to dynamic self-stabilizing cell polarity. *Development*, 144(19):3405–3416, 2017.

Li, X., Lowengrub, J., A., R., and Voigt, A. Solving PDE's in complex geometries: A diffuse domain approach. *Commun. Math. Sci.*, 7:81–107, 2009.

Maroudas-Sacks, Y., Garion, L., Shani-Zerbib, L., Livshits, A., Braun, E., and Kere, K. Topological defects in the nematic order of actin fibres as organization centres of hydra morphogenesis. *Nature Physics*, 17:251–259, 2021.

Mayer, M., Depken, M., Bois, J. S., Jülicher, F., and Grill, S. W. Anisotropies in cortical tension reveal the physical basis of polarizing cortical flows. *Nature*, 467(7315):617–621, 2010.

McCarter, J., Bartlett, B., Dang, T., and Schedl, T. On the control of oocyte meiotic maturation and ovulation in caenorhabditis elegans. *Developmental Biology*, 205:111–128, 1999.

Mesnard, D., Filipe, M., Belo, J. A., and Zernicka-Goetz, M. The anterior-posterior axis emerges respecting the morphology of the mouse embryo that changes and aligns with the uterus before gastrulation. *Current Biology*, 14(3):184–196, 2004. doi: https://doi.org/10.1016/j.cub.2004.01.026.

Mittasch, M., Gross, P., Nestler, M., Fritsch, A. W., Iserman, C., Kar, M., Munder, M., Voigt, A., Alberti, S., Grill, S. W., et al. Non-invasive perturbations of intracellular flow reveal physical principles of cell organization. *Nature Cell Biology*, 20(3):344–351, 2018.

Miyazaki, M., Chiba, M., Eguchi, H., Ohki, T., and Ishiwata, S. Cell-sized spherical confinement induces the spontaneous formation of contractile actomyosin rings in vitro. *Nature Cell Biology*, 17(4):480–489, 2015.

Motegi, F. and Seydoux, G. The par network: redundancy and robustness in a symmetry-breaking system. *Philosophical Transactions of the Royal Society B*, 368(1629):20130010, 2013.

Motegi, F., Zonies, S., Hao, Y., Cuenca, A. A., Griffin, E., and Seydoux, G. Microtubules induce self-organization of polarized par domains in caenorhabditis elegans zygotes. *Nature Cell Biology*, 13(11):1361–1367, 2011.

Munro, E., Nance, J., and Priess, J. R. Cortical flows powered by asymmetrical contraction transport par proteins to establish and maintain anterior-posterior polarity in the early c. elegans embryo. *Developmental Cell*, 7(3):413–424, 2004.

Münster, S., Jain, A., Mietke, A., Pavlopoulos, A., Grill, S. W., and Tomancak, P. Integrin-mediated attachment of the blastoderm to the vitelline envelope impacts gastrulation of insects. *BioRxiv*, page 421701, 2018.

Najafabadi, F. R., Leaver, M., and Grill, S. W. Orchestrating non-muscle myosin ii filament assembly at the onset of cytokinesis. *Molecular Biology of the Cell*, pages mbc–E21, 2022.

Nestler, M. and Voigt, A. Active nematodynamics on curved surfaces - the influence of geometric forces on motion patterns of topological defects. *Commun. Comput. Phys.*, 31:947–965, 2022.

Nestler, M., Nitschke, I., and Voigt, A. A finite element approach for vector- and tensor-valued surface PDEs. *Journal of Computational Physics*, 389:48–61, 2019. doi: 10.1016/j.jcp.2019.03.006.

Nigon, V., Guerrier, P., and Monin, H. L'architecture polaire de l'oeuf et les mouvements des constituants cellulaires au cours des premières étapes du développement chez quelques nématodes. *Bull. Biol. Fr. Belg*, 93:131–202, 1960.

Nitschke, I., Nestler, M., Praetorius, S., Löwen, H., and Voigt, A. Nematic liquid crystals on curved surfaces: a thin film limit. *Proc. Roy. Soc. A*, 474:20170686, 2018.

Nitschke, I., Reuther, S., and Voigt, A. Hydrodynamic interactions in polar liquid crystals on evolving surfaces. *Phys. Rev. Fluids*, 4:044002, 2019.

Nitschke, I., Reuther, S., and Voigt, A. Liquid crystals on deformable surfaces. *Proc. Roy. Soc. A*, 476:20200313, 2020.

Nitschke, I., Sadik, S., and Voigt, A. Tangential tensor fields on deformable surfaces – how to derive consistent L^2-gradient flows. *arXiv:2209.13272v1*, 2022.

Niwayama, R., Shinohara, K., and Kimura, A. Hydrodynamic property of the cytoplasm is sufficient to mediate cytoplasmic streaming in the caenorhabiditis elegans embryo. *Proceedings of the National Academy of Sciences*, 108(29):11900–11905, 2011.

O'Connell, K. F., Maxwell, K. N., and White, J. O. The spd-2 gene is required for polarization of the anteroposterior axis and formation of the sperm asters in the caenorhabditis elegans zygote. *Developmental Biology*, 222(1):55–70, 2000.

Piekny, A. J. and Mains, P. E. Rho-binding kinase (let-502) and myosin phosphatase (mel-11) regulate cytokinesis in the early caenorhabditis elegans embryo. *Journal of Cell Science*, 115(11):2271–2282, 2002.

Prost, J., Jülicher, F., and Joanny, J. F. Active gel physics. *Nature Physics*, 11:111–117, 2015.

Reymann, A.-C., Staniscia, F., Erzberger, A., Salbreux, G., and Grill, S. W. Cortical flow aligns actin filaments to form a furrow. *Elife*, 5:e17807, 2016.

Riddle, D. L., Blumenthal, T., Meyer, B. J., and Priess, J. R. *C. Elegans Ii*. Cold spring harbor laboratory press, 1997.

Rose, L. and Gönczy, P. Polarity establishment, asymmetric division and segregation of fate determinants in early c. elegans embryos. *WormBook*, (ARTICLE), 2014.

Rose, L. S., Lamb, M. L., Hird, S. N., and Kemphues, K. J. Pseudocleavage is dispensable for polarity and development in c. elegans embryos. *Developmental Biology*, 168(2):479–489, 1995.

Sagy, N., Slovin, S., Allalouf, M., Pour, M., Savyon, G., Boxman, J., and Nachman, I. Prediction and control of symmetry breaking in embryoid bodies by environment and signal integration. *Development*, 146(20), 10 2019. doi: 10.1242/dev.181917. dev181917.

Salbreux, G., Prost, J., and Joanny, J. F. Hydrodynamics of cellular cortical flows and the formation of contractile rings. *Phys. Rev. Lett.*, 103:058102, Jul 2009. doi: 10.1103/PhysRevLett.103.058102.

Salbreux, G., Charras, G., and Paluch, E. Actin cortex mechanics and cellular morphogenesis. *Trends in Cell Biology*, 22(10):536–545, 2012.

Salbreux, G., Jülicher, F., Prost, J., and Callan-Jones, A. Theory of nematic and polar active fluid surfaces. *Phys. Rev. Res.*, 4:033158, Aug 2022. doi: 10.1103/PhysRevResearch.4.033158.

Schonegg, S. and Hyman, A. A. Cdc-42 and rho-1 coordinate acto-myosin contractility and par protein localization during polarity establishment in c. elegans embryos. *Development*, 2006.

Shelton, C. A., Carter, J. C., Ellis, G. C., and Bowerman, B. The nonmuscle myosin regulatory light chain gene mlc-4 is required for cytokinesis, anterior-posterior polarity, and body morphology during caenorhabditis elegans embryogenesis. *The Journal of cell biology*, 146(2):439–451, 1999.

Sönnichsen, B., Koski, L., Walsh, A., Marschall, P., Neumann, B., Brehm, M., Alleaume, A.-M., Artelt, J., Bettencourt, P., Cassin, E., et al. Full-genome rnai profiling of early embryogenesis in caenorhabditis elegans. *Nature*, 434(7032):

462–469, 2005.
Tanaka, H. and Araki, T. Simulation method of colloidal suspensions with hydrodynamic interactions: Fluid particle dynamics. *Physical Review Letters*, 85(6):1338, 2000.
Tse, Y. C., Werner, M., Longhini, K. M., Labbe, J.-C., Goldstein, B., and Glotzer, M. Rhoa activation during polarization and cytokinesis of the early caenorhabditis elegans embryo is differentially dependent on nop-1 and cyk-4. *Molecular Biology of the Cell*, 23(20):4020–4031, 2012.
Vey, S. and Voigt, A. AMDiS: adaptive multidimensional simulations. *Computing and Visualization in Science*, 10(1): 57–67, 2007.
Vianello, S. and Lutolf, M. P. Understanding the mechanobiology of early mammalian development through bioengineered models. *Developmental Cell*, 48(6):751–763, 2019.
Wallenfang, M. R. and Seydoux, G. Polarization of the anterior–posterior axis of c. elegans is a microtubule-directed process. *Nature*, 408(6808):89–92, 2000.
Ward, S. and Carrel, J. S. Fertilization and sperm competition in the nematodecaenorhabditis elegans. *Developmental Biology*, 73(2):304–321, 1979.
Witkowski, T., Ling, S., Praetorius, S., and Voigt, A. Software concepts and numerical algorithms for a scalable adaptive parallel finite element method. *Advances in Computational Mathematics*, 41(6):1145–1177, 2015.
Zhang, Z., Zwick, S., Loew, E., Grimley, J. S., and Ramanathan, S. Mouse embryo geometry drives formation of robust signaling gradients through receptor localization. *Nature Communications*, 10(1):1–14, 2019.
Zonies, S., Motegi, F., Hao, Y., and Seydoux, G. Symmetry breaking and polarization of the c. elegans zygote by the polarity protein par-2. *Development*, 137(10):1669–1677, 2010.

ACKNOWLEDGEMENTS

S.W.G. was supported by the DFG (grant nos. TRR 83, GR 3271/1, GR 3271/2, GR 3271/3 and GR 3271/4) and the European Research Council (grant nos. 742712 and H2020-MSCA-ITN-2015). P.G. acknowledges a EMBO Long-Term Fellowship for funding. This work was funded by the Max Planck Society and received support from the DFG under Germany's Excellence Strategy no. EXC-2068-390729961. A.V. acknowledges support from DFG (grant no. FOR 3013). We further acknowledge computing resources provided at ZIH at TU Dresden within project WIR. We additionally thank K. Crell, T. Middelkoop, L. Pimpale, A. Narayanan and all members of the Grill Lab for experimental help and discussions. Furthermore, we thank the light microscopy facility of MPI-CBG for their support. We also thank J. White for discussions and critical inputs on the manuscript. We are grateful to P. Gönczy for comments on the manuscript.

AUTHOR CONTRIBUTIONS

This project was conceived by A.B., M.N., P.G., M.K., M.L., A.V. and S.W.G. A.B., M.K. and P.G. designed and performed all the experiments. M.N. designed and performed all the simulations. The results were analysed by A.B., M.K., P.G. and M.N. The mathematical model was conceived by M.N., P.G., A.V. and S.W.G, while the minimal model was conceived by A.B, M.L. and S.W.G. The main text was written by A.B., M.N., M.L., A.V. and S.W.G.

COMPETING FINANCIAL INTERESTS

The authors declare no competing interests.

Supplemental Information

Archit Bhatnagar, Michael Nestler, Peter Groß, Mirna Kramar, Mark Leaver, Axel Voigt, Stephan W. Grill

1 Methods

1.1 *C. elegans* strains

C. elegans strains used in this study were cultured on nematode growth media plates, seeded with OP50 *E. coli.*, as previously described (Brenner, 1974). Strains were maintained at 20 °C. The strains used in this study are listed in SI: Figure 1.

Fluorophore	Strain Name	Genotype
PAR-2::GFP, PAR-6::mCherry	TH120	(unc-119(ed3) III; ddIs25[pie-1::GFP::par-2[RNAi res. SacI/MluI])b + unc-119]; ddIs26[mCherry::T26E3.3 (par-6) + unc-119(+)])
NMY-2::GFP, PH-Domain::mCherry	SWG070	nmy-2(cp7[nmy-2::gfp + LoxP unc-119(+) LoxP]) I; ltIs44 [pAA173 pie-1p-mCherry::PH(PLC1delta1) + unc-119(+)]

SI: Table 1: *C. elegans* strains used in this study

1.2 RNA interference

All RNAi interference were performed via feeding, as previously described (Timmons et al., 2001). Briefly, RNAi feeding plates were created by seeding NGM agar plates, containing 1 mM isopropyl-β-D-thiogalactoside and 50 µg mL^{-1} ampicillin, with bacteria expressing dsRNA targeting the gene of interest. The *nop-1*, *mel-11* and *ima-3* RNAi clones were obtained from the Ahringer RNAi library (Source Bioscience) (Kamath and Ahringer, 2003). The *mlc-4* RNAi clone was obtained from the Hyman lab (Middelkoop et al., 2021). For single RNAi interference experiments, only the RNAi clone of interest was grown on the RNAi feeding plates. For double RNAi interference of *nop-1* and *mel-11*, both RNAi clones were grown simultaneously on the RNAi feeding plates. RNAi interference was then performed by transferring young L4 larvae onto these RNAi feeding plates before imaging. Indicated hours of RNAi treatment reflect the time that the worms spent on the feeding plate. See SI: Figure 2 for feeding times for each condition.

RNAi condition	Feeding time
mlc-4	22–24 hours
nop-1	24–27 hours
nop-1; *mel-11* (double)	24–27 hours
ima-3	20–24 hours

SI: Table 2: Feeding times for RNAi conditions

1.3 Microscopy details

1.3.1 Microscope Systems

All movies of *C. elegans* embryos were obtained at room temperature, using spinning-disk confocal microscopy. Two different microscope setups were used:

System 1: Zeiss Axio Observer Z1 equipped with Yokogawa CSU-X1 scan head, a PlanApochromat 63X/1.2 NA Water objective, an Andor iXon emCCD camera (512 pixel by 512 pixel), operated using Andor iQ software.

System 2: Zeiss Axio Observer Z1 equipped with Yokogawa CSU-X1 scan head, a C-Apochromat 63X/1.2 NA Water objective, a Hamamatsu ORCA-Flash4.0 V2 CMOS camera (2048 pixel by 2048 pixel), operated using Micro-Manager (Edelstein et al., 2014).

System 1 was used for all movies obtained in TH120 strain. System 2 was used for all movies obtained in SWG070 strain. Both systems utilize the same excitation laser wavelengths, namely 488 nm for GFP, and 568 nm for mCherry.

1.3.2 Mounting

C. elegans embryos were dissected from adult worms and mounted in M9 buffer (22 mM KH_2PO_4, 42 mM Na_2HPO_4, 86 mM NaCl). 20 µm polystyrene beads were added to the M9 buffer as spacers for imaging.

1.3.3 Image acquisition

System 1:

Movies of PAR domains in TH120 strain for unperturbed control and *mlc-4* RNAi embryos were acquired using System 1. At each time-point in a movie, two images were acquired at the mid-plane of the embryo - one for each channel using the corresponding excitation lasers: 488 nm for GFP and 594 nm for mCherry. For unperturbed control embryos, movies were acquired at 5 s intervals between time-points, with 80 ms exposure time for GFP and 900 ms exposure time for mCherry. For *mlc-4* RNAi embryos, movies were acquired at 10 s intervals between time-points, with 80 ms exposure time for GFP and 300 ms exposure time for mCherry. Pixel size = 0.211 µm.

System 2:

Movies of myosin in SWG070 strain for unperturbed control and all RNAi embryos were acquired using System 2. At each time-point in a movie, three images were acquired at the mid-plane of the embryo - one for each channel. One image is acquired using transmitted light (data not shown), and the rest two are acquired using the corresponding excitation lasers: 488 nm for GFP and 561 nm for mCherry. All movies were acquired at 3 s intervals between time-points, with 50 ms exposure time for transmitted light, 200 ms exposure time for GFP and 150 ms exposure time for mCherry. Pixel size = 0.105 µm.

C. elegans embryos were imaged starting from the beginning of polarizing flows until pronuclear meeting. T=0 s was selected at the end of flow phase - the time-point after which the male pronucleus moves away from the cortex and towards the female pronucleus. All movies were synchronized using this time-point. *mlc-4* RNAi embryos were synchronized using the pronuclear meeting (at T=180 s) instead, due to a lack of cortical flows in these embryos.

1.4 Image Analysis

Each movie is analysed in the following way:

1. Each movie is cropped to ensure that only a single embryo was present in each frame. Anterior and posterior end of the embryo were manually annotated. The first frame in the movie at which the male pronucleus appears and the last frame before the male pronucleus moves away from the cortex were manually selected. The male pronucleus was identified as a dark circle in the cytoplasm in the fluorescently labelled channels (PAR-2::GFP in TH120, NMY-2::GFP in SWG070), located near to the posterior end. Any embryos where both pronuclei are located near to the same end were discarded. Only frames between the first and last frame selected above were analysed. Each movie was rotated such that the anterior and posterior ends were closer to the left and right edges of the rotated image respectively, with the male pronucleus located near the bottom edge (note: the images in the micrographs shown in this study are flipped). Manual annotation and rotation were done in FIJI (Schindelin et al., 2012; Linkert et al., 2010), using bilinear interpolation.

2. To track the position of the male pronucleus as it posteriorizes, rotated movies for SWG070 strain were analysed using a custom Python (Python Core Team, 2019) script. First, the cell membrane of the embryo in each frame was segmented by thresholding, using the phDomain::mCherry marker for the cell membrane, and then fit to an ellipse. Semi-major and semi-minor axes lengths and directions of the fitted ellipses are averaged over all frames to obtain the semi-major and semi-minor axes for the embryo as a whole. Next, NMY-2::GFP channel image was denoised using non-local means denoising (Buades et al., 2011), with the following parameters: Filter strength = 3 pixel, template window size = 4 pixel, search window size = 12 pixel. Next, the male pronucleus was segmented in these denoised NMY-2::GFP frames using successive thresholding - the male pronucleus was identified as a dark circle in the cytoplasm, present in the right half of the embryo. Thesae segmentations were verified manually. Finally, the trajectory of the male pronucleus was obtained by noting the position of the male pronucleus, as segmented, as a function of number of frames, and therefore time. Posteriorization velocities were calculated as the component of male pronucleus velocity perpendicular to the line connecting the male pronucleus center to the closest point on the cell membrane. Following additional packages were used in this Python script: openCV (Bradski, 2000), tifffile (Gohlke, 2019), scipy (Virtanen et al., 2020), numpy (Harris et al., 2020), pandas (McKinney, 2010) and matplotlib (Hunter, 2007). For movies with TH120 strain, no boundary segmentations were done. Male pronucleus was identified manually using a custom FIJI (Schindelin et al., 2012) macro, in a similar fashion to the automatic Python script.

3. Cortical flow fields were only determined in SWG070 strain embryos using a custom MATLAB (MATLAB, 2016) script, as previously described in Gross et al. (2019). Briefly, cortical flows were determined by calculating the displacement field of the yolk granules near the cell membrane in NMY-2::GFP denoised frame, using PIVlab algorithm in MATLAB (Thielicke and Stamhuis, 2014). The displacement field was calculated for each frame, in a region extending 3.15 µm = 30 pixel deep in the embryo and perpendicular to the cell membrane. These 2D velocity fields were binned and projected onto the cell

membrane, thus yielding the measured cortical flows for each frame in the movie. A multi-pass (4 passes) PIV was utilized in all cases, with initial template size of 2.52 µm = 24 pixel and step size of 0.42 µm = 4 pixel.

For unperturbed control and *ima-3* RNAi embryos (SWG070 strain), myosin concentrations in the cytosol and cortex were also calculated, in intensity per pixel units. Intensity is measured in arbitrary units, corresponding to the camera readings in the movies. Cortex is identified as a region 15 pixel = 1.6 µm deep from the cell membrane. Cytosol is identified as the interior region of the embryo, left after the cortical region is removed. Myosin concentration in each region is estimated as the average intensity per pixel in the corresponding region. See SI: Figure 11 for comparison.

1.5 Data analysis

The above image analysis pipeline provides the angular position of the male pronucleus, posteriorization velocity and cortical flows for each frame in each movie. This data is then analysed in the following way:

Posteriorization velocity vs angular position graphs

To smooth short-term fluctuations in posteriorization velocity and angular position, a sliding average with a window of 7 frame is used for each movie. Then, all posteriorization velocities and angular positions from all movies in the condition of interest are combined together. Angular positions are binned in 3 deg bins. Mean posteriorization velocity for each angular position bin is calculated by averaging over all posteriorization velocities corresponding to the angular positions included in the bin. 95% confidence interval for the mean posteriorization velocities are calculated using a two-sided t-test.

Cortical flows

Cortical flows for all movies in the condition of interest are combined together, and binned by the angular position of the male pronucleus, with 3 deg bin width. The mean cortical flows for an angular position bin are calculated by averaging all cortical flows within an angular position bin. Cortical flows are averaged spatially - i.e., average flow velocity at a certain point on the cortex is calculated by averaging over all observed flow velocities at that point. See subsection 2.2 for calibration of model parameters using these averaged cortical flows.

2 Modeling

2.1 Mechanical Feedback Loop

To obtain a theoretical description for the convergence of body axes to embryo shape we define a feedback loop, connecting mechanical processes in cortex and cytoplasm. First contribution in this loop are flows and actin alignment in the cortex. These intertwined effects are driven by gradients in myosin distribution due to a localized depletion in cortical layer triggered by the centrosome. Second contribution comes from these cortical flows driving cytoplasmic flows, yielding an advective transport and drag of the nucleus and thereby the attached centrosome. With the centrosomal trigger displaced the myosin distribution rearranges, cortical activity and flow profiles are displaced as well and the loop is closed.

In our modelling we neglect temporal minor fluctuations in the cell shape and considered the shape as a fixed spherical ellipsoid with typical in-vivo dimensions $[a, b, c] = [28.7\mu m, 16.4\mu m, 16.4\mu m]$. The cortical layer is assumed as a thin film enveloping the cytoplasmic bulk with constant thickness $h \ll a$. We denote $\mathcal{E}$ as surface of the ellipsoid and $\hat{\mathcal{E}}$ the enclosed bulk. For these two domains, cortical layer and enclosed cytoplasmic bulk, we apply a coarse-grained/continuous modeling framework laid out in (Jülicher et al., 2018) to obtain a suitable model for each domain. Due to the intricate physics of the cortex and its curved thin film geometry we will focus the modeling discussion on this part of the feedback loop. Furthermore, to separate the modeling assumptions and the impacts of confined geometries and its curvature we derive the cortex model in three steps. As initial step we discuss two established models of (Gross et al., 2019) and (Reymann et al., 2016) as well as their experimentally determined phenomenological parameters for an apriori estimate of dominant effects. In the second step we will derive a model for the cortex physics in an unbounded, volume like bulk domain, following the approach of (Jülicher et al., 2018). As third step we transfer the volume model to a bounded thin film domain (thickness h), discuss boundary conditions and perform the thin film limit $h \to 0$ (Nitschke et al., 2020; Arroyo and DeSimone, 2009) to obtain the final cortex model. For the remaining feedback loop contributions, cytoplasmic streaming and nucleus transport, we will straight forward apply established models of (Niwayama et al., 2011; Tanaka and Araki, 2000). For sake of numerical feasibility, we consider the coupling between cortex and cytoplasm as "one way", enabling a sequential evaluation of the associated models.

2.1.1 Cortical mechanics

A prior consideration The cortical layer and its governing physics are subject of an extended research providing a wide range of experimental observations and theoretical descriptions. For our modeling we will use two recent models as building blocks as well as their experimental observations as guiding concepts.

As first building block we use the results of (Gross et al., 2019) which provides a description of the interplay of myosin depletion, flows due to myosin gradients and forming of PAR domains as a bistable system. We will neglect the formation of PAR domains and take from this model the connection of myosin depletion and cortical force generation. Reviewing the determined phenomenological parameters we observe that myosin concentration is dominated by un-binding dynamics between cortex and cytoplasmic bulk. Furthermore the observed cortical flow field is of compressible nature driven only by forces due to myosin gradients. Please note due to the limitation to one dimensional domain and absence of curvature the model is invariant under translation such that a displacement of the centrosome yields a quasi instantaneous, equivalent displacement in myosin and flow fields. Second building block in modeling cortical dynamics are the results of (Reymann et al., 2016). There it has been established how compression of actin filaments yield a localized, ribbon like domain with aligned filaments. Such local aligned filaments, in combination with myosin motors, exert forces normal to the cortical layer yielding the ingression of the pseudocleavage furrow. Key mechanism in the model, driving the localized alignment, is the reactive coupling between deviatoric stresses and filament alignment. The results of (Reymann et al., 2016) consider this coupling as one way connection, neglecting any effects of alignment on cortical flow fields. Furthermore a cylinder like domain and rotational symmetric flow field and alignment are considered such that only normal (w.r.t cylinder domain) forces are yielded. Here we will use the modelling approach but focus on the tangential parts of the force generation and neglect the normal parts. Furthermore the considered ellipsoidal domain yields a significant different curvature distribution compared to a cylinder.

For the subsequent modeling we will combine these two approaches, along the concepts of (Jülicher et al., 2018), to obtain a cortex model coupling momentum balance, with flows driven by forces due to myosin gradients as well as due to localized actin alignment, and alignment induced by flow compression. To estimate the impact of possible coupling mechanisms we review the experimental observations and calibrated phenomenological parameters of (Reymann et al., 2016). There the actin alignment is described by the uniaxial nematic order parameter $\mathbf{Q}$ (De Gennes and Prost, 1993) with flux $D^c\mathbf{Q}/Dt$ and adjoint force $\mathbf{H}$. The nematic state equation (3) is rescaled along a characteristic nematic relaxation time $\tau = \Gamma/A$ (nematic dissipation rate versus nematic energy density) and a nematic distortion length $\lambda_D = \sqrt{L/A}$ (nematic elastic coefficient versus nematic energy density). Observations in (Reymann et al., 2016) indicate a relaxation time below measurement resolution, such that we will neglect flux contributions to nematic state equations. Furthermore, we use the observed values of $\lambda_D = 4.72$ and $\|\mathbf{Q}\| = \mathcal{O}(0.1)$ to estimate the order of magnitude for possible nematic stress contributions to the momentum balance. We yield $\|\mathbf{H}\| = A\mathcal{O}(0.1)$ for alignment stress and $\|\mathbf{QH} - \mathbf{HQ}\| = A\mathcal{O}(0.01)$, $\|A\,\lambda_D^2 \nabla\mathbf{Q} : \nabla\mathbf{Q}\| = A\mathcal{O}(0.01)$ for nematic anti symmetric and equilibrium stress. Assuming a weak nematic energy density $A \leq \mathcal{O}(1)$ we will neglect the anti symmetric and equilibrium stress contributions in further modeling.

Given the parameter regime specified by (Gross et al., 2019; Reymann et al., 2016) for *C. elegans* zygote during pseudocleavage, the relaxation of cortical dynamics is considered fast compared to the timescale of axis convergence.

Bulk modeling We consider the cortical layer as a fluid constituted by a mixture of rodlike particles (actin) and spherical shaped particles (myosin), with particle number densities $\mathcal{A}$ and $\mathcal{M}$.

$$\rho = m_{\mathcal{A}}\mathcal{A} + m_{\mathcal{M}}\mathcal{M} \tag{1}$$

Actin is assumed to be uniformly distributed ($\mathcal{A} \approx \text{const}$) in the domain varying only in the degree of local ordering (Reymann et al., 2016). Myosin motor distribution is assumed to exhibit temporal and spatial patterns mainly driven by local depletion near centrosome position $\mathbf{x}_N$ and un/rebinding bulk (Gross et al., 2019). Possible gradients of $\mathcal{M}$ in the neighboring cytoplasmic bulk, as discussed in (Geßele et al., 2018), as well as advective transport are neglected. Following (Gross et al., 2019), the particle number density balance reads therefore

$$-D_{\mathcal{M}}\nabla\cdot\nabla\mathcal{M} = \kappa_{on}\mathcal{M}^* - \kappa_{off}\mathcal{M} - \kappa_{\mathcal{M}}\kappa_{off}f(\mathbf{x}_N)\mathcal{M} \tag{2}$$

where total amount of myosin is conserved by $\mathcal{M}^* = \mathcal{M}^{tot} - \psi/|\Omega|\int_\Omega \mathcal{M}\,\mathrm{d}\Omega$ and $f(\mathbf{x}_N) = -\exp\big(-\|\mathbf{x}-\Pi_{\mathcal{E}}[\mathbf{x}_N]\|^2/d_{\mathcal{M}}^2\big)$ models the depletion near $\Pi_{\mathcal{E}}[\mathbf{x}_N]$ with radius $d_{\mathcal{M}}$. $\Pi_{\mathcal{E}}[\mathbf{x}_N]$ refers to the point in the domain Ω closest to the nucleus while ψ denotes the volume to neighbouring bulk ratio to balance the myosin reservoir.

Following (Reymann et al., 2016; Jülicher et al., 2018) the nematic alignment of actin is described by hydrodynamic variables $\mathbf{Q}$ and $\mathbf{H}$ along the state equation

$$\frac{D^c\mathbf{Q}}{Dt} = \Lambda\mathbf{D} + \frac{1}{\Gamma}\mathbf{H}, \quad \mathcal{F}^\Omega(\mathbf{Q}) = A\int_\Omega \frac{\lambda_D^2}{2}\|\nabla\mathbf{Q}\|^2 + \frac{1}{2}\|\mathbf{Q}\|^2\,\mathrm{d}\Omega, \quad \mathbf{H} = -\frac{\delta\mathcal{F}^\Omega}{\delta\mathbf{Q}} \tag{3}$$

with Λ the dimensionless parameter determining the strength of reactive flow-alignment coupling, the deviatoric (symmetric and trace free) deformation tensor of cortical flows $\mathbf{D} = [\nabla\mathbf{V} + \nabla\mathbf{V}^T]/2 - [\nabla\cdot\mathbf{V}]/3\,\mathbb{I}$ and $\mathcal{F}^\Omega$ a Landau-de Gennes like free energy describing the actin molecules tendency towards isotropic ordering and parallel alignment in case of ordering. In the considered parameter regime of fast cortical dynamics we yield

$$0 = \Lambda\tau\mathbf{D} + \frac{1}{A}\mathbf{H}, \quad \mathbf{H} = A\left[\lambda_D^2\nabla\cdot\nabla\mathbf{Q} - \mathbf{Q}\right] \tag{4}$$

For momentum balance we use the approach of (Gross et al., 2019) for velocity $\mathbf{V}$ with friction γ, as representative for momentum transfer to neighboring bulk, and active force creation due to gradients in $\mathcal{M}$

$$-\nabla\cdot\boldsymbol{\sigma} + \gamma\mathbf{V} = \tilde{\xi}\nabla\mathcal{M} \tag{5}$$

Due to the modulations in $\mathcal{M}$ we can not assume constant density, such that $\nabla\cdot\mathbf{V} \neq 0$. The viscous stress therefore contains shear and bulk contributions, with associated viscosity η (shear), η^B (bulk) and secondary viscosity $\eta^S = \eta^B + 2/3\eta$.

$$\boldsymbol{\sigma}^{visc} = \eta\left(\nabla\mathbf{V} + \nabla\mathbf{V}^T\right) + \eta^B\left(\nabla\cdot\mathbf{V}\right)\mathbb{I}_3 = 2\eta\mathbf{D} + \eta^S\left(\nabla\cdot\mathbf{V}\right)\mathbb{I}_3 \tag{6}$$

We expand this approach by incorporating the rodlike nature of actin filaments, its local alignment and active tension in alignment direction in the stress modeling, following (Jülicher et al., 2018) and the discussion above. We yield for total stress

$$\boldsymbol{\sigma} = 2\eta\mathbf{D} + \left(\eta^S\nabla\cdot\mathbf{V} - p\right)\mathbb{I} - \Lambda\mathbf{H} + \psi\triangle\mu\mathbf{Q}, \tag{7}$$

with additional phenomenological parameter ψ for active tension strength. Furthermore we assume a shear-bulk viscosity relation of $\eta^B = -2/3\eta$ and linear isentropic pressure $p \approx C_p\rho$. Therefore the momentum balance reads

$$-\eta\left[\nabla\cdot\nabla\mathbf{V} + \frac{1}{3}\nabla\nabla\cdot\mathbf{V}\right] + \gamma\mathbf{V} = \underbrace{\xi\nabla\mathcal{M}}_{(A)} + \underbrace{\psi\nabla\cdot(\triangle\mu\mathbf{Q}) - \Lambda\nabla\cdot\mathbf{H}}_{(N)} \tag{8}$$

with the two force generating mechanisms of isotropic force generation due to myosin activity (A), rescaled by $\xi = \tilde{\xi} + C_p m_{\mathcal{M}}$, and stresses due to actin alignment (N).

Thin film limit To derive now the relevant surface model from the bulk formulation of (2), (4) and (8) we follow the thin film limit approach described in detail at (Nitschke et al., 2018). There, the basic idea is to consider a tubular extension $\mathcal{E}_h$ of surface $\mathcal{E}$ with constant thickness h. In this volume $\mathcal{E}_h$ we use the previously derived bulk model endowed with physical meaningful boundary conditions on $\partial\mathcal{E}_h$ and perform the limit $h \to 0$. By using the thin film metric of $\mathcal{E}_h$ as a bridge between bulk and surface domain we yield a compatible and covariant surface model. We highlight that in the process of thin film limit the tensorial degree of the considered physical field as well as the boundary conditions are decisive for the resulting coupling of geometry and physics in the surface model. See (Nestler et al., 2020) for a detailed discussion for nematic ordering.

Given the results of (Nitschke et al., 2020; Arroyo and DeSimone, 2009) we choose boundary conditions for the bulk model. With $\boldsymbol{\nu}$ the outward pointing normal of $\mathcal{E}$, $\boldsymbol{\nu}_h$ the constant extension (in normal direction) of $\boldsymbol{\nu}$ to $\mathcal{E}_h$, $\Pi[.]$ the tangential projection to the tangent space of $\mathcal{E}$ and $\Pi_h[.]$ for $\partial\mathcal{E}_h$, we impose

- $\nabla\mathcal{M}\cdot\boldsymbol{\nu}_h = 0$, no additional flux across $\partial\mathcal{E}_h$ beside the contributions by binding dynamics
- $\mathbf{V}\cdot\boldsymbol{\nu}_h = 0$, no flow across $\partial\mathcal{E}_h$ and $\nabla_{\boldsymbol{\nu}}\mathbf{V} = 0$ no variations of velocity in normal direction.
- $\Pi_h[\boldsymbol{\sigma}\cdot\boldsymbol{\nu}_h] = 0$, normal components of stress do not contain tangential parts. Under this condition momentum balance of tangential and normal components decouple.
- $\boldsymbol{\nu}_h\cdot\mathbf{Q}\cdot\boldsymbol{\nu}_h = 0$, no nematic ordering in normal direction which is suitable for mono layers of filaments, see (Nestler et al., 2020). Furthermore we require $\nabla\mathbf{Q}\cdot\boldsymbol{\nu}_h = 0$ which ensures continuous values of $\mathbf{Q}$ in $h\to 0$.

Denoting the covariant differential operators on $\mathcal{E}$ by div and grad the thin film limit yields for myosin particle number balance

$$-D_{\mathcal{M}}\mathrm{div}\ \cdot\mathrm{grad}\,\mathcal{M} = \kappa_{on}\mathcal{M}^* - \kappa_{off}\mathcal{M} - \kappa_{\mathcal{M}}\kappa_{off}f(\mathbf{x}_N)\mathcal{M} \tag{9}$$

where $\mathcal{M}^* = \mathcal{M}^{tot} - \psi/|\mathcal{E}|\int_{\mathcal{E}}\mathcal{M}\,\mathrm{d}\mathcal{E}$, $f(\mathbf{x}_N) = -\exp\big(-s(\mathbf{x},\Pi_{\mathcal{E}}[\mathbf{x}_N])^2/d_{\mathcal{M}}^2\big)$ with a geodesic distance measure s on $\mathcal{E}$ applied and $\Pi_{\mathcal{E}}[\mathbf{x}_N]$ denotes the closest point on the cortex w.r.t to nucleus center. We denote the tangential part by lower case letters, e.g. $\Pi[\mathbf{V}|_{\mathcal{E}}] = \mathbf{v}$. Under the chosen boundary conditions, we yield for $h\to 0$ for velocity divergence $\nabla\cdot\mathbf{V}\to\mathrm{div}\,\mathbf{v}$. Please note that in the transition from volume to surface the notion of trace changes, so the surface deviatoric deformation tensor is given by $\mathbf{d} = [\mathrm{grad}\,\mathbf{v} + \mathrm{grad}\,\mathbf{v}^T]/2 - [\mathrm{div}\,\mathbf{v}]/2\mathbf{g}$, where $\mathbf{g}$ denotes the metric of $\mathcal{E}$. Therefore the thin film limit of deviatoric deformation includes an additional term. We express this term by using the augmenting surface metric (the so called thin film metric) $\mathbf{G} = \mathbf{g} + \boldsymbol{\nu}\boldsymbol{\nu}$

$$\begin{aligned}\Pi[\mathbf{D}|_{\mathcal{E}}] &= \mathbf{d} - \frac{1}{2}\left(\boldsymbol{\nu}\cdot\mathbf{D}\cdot\boldsymbol{\nu}\right)\mathbf{g} = \mathbf{d} - \frac{1}{2}\left(\nabla_{\boldsymbol{\nu}}(\mathbf{V}\cdot\boldsymbol{\nu}) - \frac{1}{3}(\nabla\cdot\mathbf{V})\boldsymbol{\nu}\cdot\mathbf{G}\cdot\boldsymbol{\nu}\right)\mathbf{g}\\ &\to \mathbf{d} + \frac{1}{6}\left(\mathrm{div}\,\mathbf{v}\right)\mathbf{g}\ \text{for}\ h\to 0\end{aligned} \tag{10}$$

Due to the boundary condition chosen for nematics such additional term does not occur for nematic ordering and molecular field. Therefore we define the tangential parts of nematic order tensor $\Pi[\mathbf{Q}|_{\mathcal{E}}] = \mathbf{q}$ and molecular field $\Pi[\mathbf{H}|_{\mathcal{E}}] = \mathbf{h}$. With $\mathcal{K}$ the Gaussian curvature, $\mathbf{B} = -\Pi[\nabla\boldsymbol{\nu}]$ the shape operator of $\mathcal{E}$ we obtain the thin film limit of nematic free energy, see (Nitschke et al., 2018), via $1/h\,\mathcal{F}^{\mathcal{E}_h}(\mathbf{Q})\to\mathcal{F}^{\mathcal{E}}(\mathbf{q})$.

$$\mathcal{F}^{\mathcal{E}}(\mathbf{q}) = A\int_{\mathcal{E}}\frac{\lambda_D^2}{2}\left[\|\mathrm{grad}\,\mathbf{q}\|^2 + \|\mathbf{B}\|^2\|\mathbf{q}\|^2\right] + \frac{1}{2}\|\mathbf{q}\|^2\,\mathrm{d}\mathcal{E},\quad \mathbf{h} = -\frac{\delta\mathcal{F}^{\mathcal{E}}}{\delta\mathbf{q}} \tag{11}$$

and nematic state equation on the surface

$$0 = \Lambda\tau\mathbf{d} + \left(\lambda_D^2\left[\mathrm{div}\,\mathrm{grad}\,\mathbf{q} - \|\mathbf{B}\|^2\mathbf{q}\right] - \mathbf{q}\right) \tag{12}$$

The total stress for $h\to 0$ reads therefore

$$\boldsymbol{\sigma}^{\mathcal{E}} = 2\eta\mathbf{d} + \frac{1}{3}\eta\mathrm{div}\,\mathbf{v}\mathbf{g} - p\mathbf{g} - \Lambda\mathbf{h} + \psi\triangle\mu\mathbf{q} \tag{13}$$

Using the previous isentropic pressure approximation and the results of (Arroyo and DeSimone, 2009), the tangential part of momentum balance on $\mathcal{E}$ reads

$$-\eta\left[\mathrm{div}\,\mathrm{grad}\,\mathbf{v} + \mathcal{K}\mathbf{v} + \frac{1}{3}\mathrm{grad}\,\mathrm{div}\,\mathbf{v}\right] + \gamma\mathbf{v} = \xi\mathrm{grad}\,\mathcal{M} + \psi\mathrm{div}\ (\triangle\mu\,\mathbf{q}) - \Lambda\mathrm{div}\,\mathbf{h} \tag{14}$$

2.1.2 Cytoplasmic bulk and nucleus transport

Following the results of (Niwayama et al., 2011) we model the cytoplasmic bulk as an Newtonian fluid in Stokes regime yielding a parameter free model. We neglect all cell organelles except the nucleus, which is described by a smooth density function $\phi(\mathbf{x}) = [1 - \tanh(3(\|\mathbf{x}-\mathbf{x}_N\| - r_N)/\epsilon)]/2$ with r_N the nucleus radius and ϵ the density transition width. By (Tanaka and Araki, 2000) we include the nucleus in the Stokes model as a region of significantly increased viscosity ($\omega_N = 100$) enforcing a homogeneous flow field inside the nucleus. The drag induced by cortical activity is modelled by a velocity boundary condition. Therefore the cytoplasmic bulk model for bulk velocity $\mathbf{U}$ and pressure P reads

$$\begin{aligned}-\nabla\cdot\left((1+\omega_N\phi)\,\nabla\mathbf{U}\right) + \nabla P &= 0 \quad \text{in}\ \hat{\mathcal{E}}\\ \nabla\cdot\mathbf{U} &= 0 \quad \text{in}\ \hat{\mathcal{E}}\\ \mathbf{U} &= \mathbf{v} \quad \text{on}\ \mathcal{E}\end{aligned} \tag{15}$$

The nucleus velocity $\mathbf{U}_N$ is then calculated from two contributions. First contribution is the advective transport by cytoplasmic streaming. Here we evaluate the tangential part, w.r.t. ellipsoid normal $\boldsymbol{\nu}_N$ at closest point on the cortex $\Pi_{\mathcal{E}}[\mathbf{x}_N]$, of the average cytoplasmic velocity in nucleus domain

$$\tilde{\mathbf{U}}_N^1 = \int_{\hat{\mathcal{E}}}\phi\mathbf{U}\,\mathrm{d}\hat{\mathcal{E}}\ /\int_{\hat{\mathcal{E}}}\phi\,\mathrm{d}\hat{\mathcal{E}},\quad \mathbf{U}_N^1 = \tilde{\mathbf{U}}_N^1 - \left(\tilde{\mathbf{U}}_N^1\cdot\boldsymbol{\nu}_N\right)\boldsymbol{\nu}_N \tag{16}$$

The second contribution roots in the drag of the nucleus due to local movement of the cortical layer. For this purpose we evaluate an average cortical velocity across a domain matching the projection of the nucleus on the cortex. Again we only consider the tangential contribution

$$\mathcal{N} = \{\mathbf{x} \in \mathcal{E} \,:\, \|\,(\mathbf{x} - (\mathbf{x}\cdot\boldsymbol{\nu}_N)\boldsymbol{\nu}_N) - \Pi_{\mathcal{E}}[\mathbf{x}_N]\| \leq r_N\},$$
$$\tilde{\mathbf{U}}_N^2 = \int_{\mathcal{N}} \mathbf{v}\,\mathrm{d}\mathcal{N}/|\mathcal{N}|, \quad \mathbf{U}_N^2 = \tilde{\mathbf{U}}_N^2 - \left(\tilde{\mathbf{U}}_N^2 \cdot \boldsymbol{\nu}_N\right)\boldsymbol{\nu}_N \tag{17}$$

Since the strength of cortical drag is unknown we introduce a phenomenological factor $d \in [0,1]$. Such modelling could be understood as basic approximation of the interaction of cortex and cytoplasmic bulk in normal direction. The evolution of nucleus position reads therefore

$$\dot{\mathbf{x}}_N = \mathbf{U}_N^1(\mathbf{x}_N) + d\mathbf{U}_N^2(\mathbf{x}_N) \tag{18}$$

2.2 Parameter calibration

Before starting parameter calibration we will review the cortex model regarding the included phenomenological parameters and available experimental data to arrive at an feasible calibration problem. Furthermore we remove units from the complete feedback cycle by dedimensionalizing the state equations (9),(14) and (15) along characteristic time 1 s and 1 µm.

Cortex model review In the given parameter regime we can rewrite the nematic state equation (12) and yield $\mathbf{h} = -\Lambda\tau\mathbf{d}$ resulting in a strong similarity in force fields of associated viscous and flow alignment stresses. Furthermore, we lack the experimental data to effectively discriminate the contributions of viscous and alignment forces. We therefore define and calibrate an effective viscosity $\tilde{\eta}$ accounting for the combined effect.

$$\tilde{\eta}\,\mathrm{div}\,\left[2\mathbf{d} + \frac{1}{3}\mathrm{div}\,\mathbf{v}\mathbf{g}\right] \approx \mathrm{div}\,\left[2\eta\mathbf{d} + \frac{1}{3}\eta\mathrm{div}\,\mathbf{v}\mathbf{g}\right] - \Lambda\,\mathrm{div}\,[\mathbf{h}] \tag{19}$$
$$= \eta\mathrm{div}\,\left[2\mathbf{d} + \frac{1}{3}\mathrm{div}\,\mathbf{v}\mathbf{g}\right] + \frac{\Lambda^2\tau a}{2}\,\mathrm{div}\,[2\mathbf{d}] \tag{20}$$

Reviewing the active nematic force contribution $\psi\mathrm{div}\,(\triangle\mu\,\mathbf{q})$ we observe the presence of contributions parallel to viscous forces. To reduce the "overlap" in these force contributions we follow (Reymann et al., 2016) and consider only active stresses along the nematic ribbon.

$$\boldsymbol{\sigma}^{ribbon} = \psi\triangle\mu\left[\frac{1}{2\sqrt{2}}\|\mathbf{q}\|\mathbf{g} + \frac{1}{2}\mathbf{q}\right] \tag{21}$$

Finally we highlight that (Gross et al., 2019) applies a slightly different approach in modeling isotropic active forces by $\xi^*\mathrm{grad}\triangle\mu$ (instead of $\xi\mathrm{grad}\,\mathcal{M}$) where $\triangle\mu = \mathcal{M}/\left[\mathcal{M} + \mathcal{M}^*\right]$. Applying such modeling indeed improved the reproduction of cortical flow field data. Therefore we adapt this modeling for the chemical potential and apply it also in the prefactor of active stress along the nematic ribbon.

Given this refined modeling, we follow Gross et al. (2019); Reymann et al. (2016) and cancel friction by introducing cortical hydrodynamic length $\lambda_H = \sqrt{\tilde{\eta}/\gamma}$ as well as a nematic stress relaxation $\lambda_N = \psi/\gamma$ and active force relaxation $\lambda_A = \xi^*/\gamma$. The cortical particle numbers for Myosin, momentum balance and nematic state equation read therefore

$$-D_{\mathcal{M}}\mathrm{div}\,\cdot\,\mathrm{grad}\,\mathcal{M} = \kappa_{on}\mathcal{M}^* - \kappa_{off}\mathcal{M} - \kappa_{\mathcal{M}}\kappa_{off}f(\mathbf{x}_N)\mathcal{M}$$
$$-\lambda_H^2\,\left[\mathrm{div}\,\mathrm{grad}\,\mathbf{v} + \mathcal{K}\mathbf{v} + \frac{1}{3}\mathrm{grad}\,\mathrm{div}\,\mathbf{v}\right] + \mathbf{v} = \lambda_N\,\mathrm{div}\,\left[\frac{\triangle\mu}{2\sqrt{2}}\|\mathbf{q}\|\mathbf{g} + \frac{\triangle\mu}{2}\mathbf{q}\right] + \lambda_A\,\mathrm{grad}\,\triangle\mu \tag{22}$$
$$0 = \Lambda\tau\mathbf{d} + \left(\lambda_D^2\left[\mathrm{div}\,\mathrm{grad}\,\mathbf{q} - \|\mathbf{B}\|^2\mathbf{q}\right] - \mathbf{q}\right)$$

Please note, that $(\mathbf{v},\mathbf{q})$ scale with λ_A, e.g. $\tilde{C}\lambda_A \to (\tilde{C}\mathbf{v}, \tilde{C}\mathbf{q})$, enabling us to fit λ_A separately by requiring to match kinetic energy in model cortex flow fields with experimental data.

Using parameter values for the Myosin and nematic state equation as specified in Gross et al. (2019); Reymann et al. (2016) only the two parameters λ_H and λ_N need to be calibrated.

Calibration for unperturbed control embryos The calibration procedure for the cortex model uses experimental data of cortical flow profiles on a planar slice of $\mathcal{E}$. Such profiles $\mathbf{v}^d(\alpha_i)$ are available for a set of nucleus positions $\mathbf{x}_N(\alpha_i)$ with displacement angles α_i, see SI: Figure 6-[A](blue lines) for unperturbed control embryos data or SI: Figure 7(blue lines) for NOP data. The plane is determined by AP axis and nucleus center, we label the slice of the cortex by $\mathcal{P}$. The cortical velocities are described w.r.t a counter clockwise tangential direction $\mathbf{t}$ and are plotted along an oriented geodesic distance s on the ellipse with the nucleus position as origin, $s = 0$. Please note, such coordinate system corresponds to shift of the fixed coordinate system of

experimental data where $s = 0$ is always aligned with the posterior pole. We use this data to calibrate the parameters λ_H, λ_N, λ_A of cortical model in a two step process.

As first step we solve (22) and obtain$(\mathcal{M}, \mathbf{v}^*, \mathbf{q}^*)$ for each α_i and for an array of values $(\lambda_H,\ \lambda_N)$ while keeping λ_A^* fixed. The value of λ_A is then determined by fitting the kinetic energy $\mathbb{E}^{\mathcal{P}}(\mathbf{v}) = \int_{\mathcal{P}} \mathbf{v}^2 \, \mathrm{d}\mathcal{P}$ across all velocity profiles

$$\min_{S\in\mathbb{R}} \sum_i \left[\mathbb{E}^{\mathcal{P}}(\mathbf{v}^d(\alpha_i)) - \mathbb{E}^{\mathcal{P}}(S\mathbf{v}^*(\alpha_i))\right] = S^*,$$
$$\lambda_A = S^*\lambda_A^*, \quad \mathbf{v}(\lambda_H,\ \lambda_N,\ \lambda_A) = S^*\mathbf{v}^*(\lambda_H,\ \lambda_N,\ \lambda_A^*) \tag{23}$$

As second step we evaluate a mixed calibration cost measure $E = L + \Theta R$ combining a similarity measure L and an imbalance measure R with weighting factor Θ. Both measures are relative w.r.t to the model results. Basic motivation for the imbalance measure is the observation of a distinct correlation of nucleus displacement α_i and the ratio of velocity magnitudes pointing towards to and away form the posterior pole. While this ratio is 1 for aligned nucleus ($\alpha = 0$) the imbalance increases with further nucleus displacement. Therefore, the imbalance measure penalizes deviations in the magnitude ratios between experimental and model data across all displacement angles. We formalize this approach by

$$L = \sum_i \sqrt{[\mathbb{E}^{\mathcal{P}}(\mathbf{v}^d(\alpha_i)) - \mathbb{E}^{\mathcal{P}}(\mathbf{v}(\alpha_i))]/\mathbb{E}^{\mathcal{P}}(\mathbf{v}(\alpha_i))} \tag{24}$$

$$M^+(\mathbf{v}) = -\frac{1}{2}\int_{\mathcal{P}} -\mathbf{v}\cdot\mathbf{t} - |\mathbf{v}\cdot\mathbf{t}| \, \mathrm{d}\mathcal{P}$$
$$M^-(\mathbf{v}) = -\frac{1}{2}\int_{\mathcal{P}} \mathbf{v}\cdot\mathbf{t} - |\mathbf{v}\cdot\mathbf{t}| \, \mathrm{d}\mathcal{P}$$
$$R = \sum_i \left|\frac{M^+(\mathbf{v}^d(\alpha_i))}{M^-(\mathbf{v}^d(\alpha_i))} - \frac{M^+(\mathbf{v}(\alpha_i))}{M^-(\mathbf{v}(\alpha_i))}\right| \Big/ \left|\frac{M^+(\mathbf{v}(\alpha_i))}{M^-(\mathbf{v}(\alpha_i))}\right| \tag{25}$$

A variation of the calibration parameter Θ demonstrates the relevance of imbalance feature. For $\Theta = 0$ the calibration results in a model failing to capture the imbalances and yield weak nucleus velocities $\mathbf{U}_N^1$ and $\mathbf{U}_N^2$. Yet choosing a high value, e.g. $\Theta = 50$, we yield model cortical flow profiles with weak similarity to experimental data. For the final error measure we use a value $\Theta = 5$ to weight the error measures.

See SI: Figure 6-[B] for the resulting calibration cost landscape for unperturbed control embryos cortical flow data. In SI: Figure 6-[A] and SI: Figure 7(red lines) we plot the velocities of best fit models and observe a good reproduction of the experimental velocities. We summarize the obtained parameter values in SI: Figure 3.

After calibrating the cortex model parameters we evaluate the cytoplasmic flows and resulting nucleus velocities due to advective transport $\mathbf{U}_N^1$ as well as cortical drag $\mathbf{U}_N^2$ for a range of displacement angles $\alpha_j \in [0, 30°]$ (10 points). We compare the model nucleus velocity contributions to the in-vivo observed nucleus velocities, see SI: Figure 6-[C]. From this comparison we determine the effective drag factor $d = 0.61$ as optimal to reproduce nucleus velocities for $\alpha \in [0, 20°]$. For stronger displacements deviations in nucleus velocities remain, regardless of the value of d.

To complement the parameter calibration we investigate the sensitivities of model parameters w.r.t. the impact on nucleus velocity. Due to linearity of $\mathbf{U}$ to boundary velocities $\mathbf{v}$ in (15) we yield equivalent change in nucleus velocity for changes in λ_A. For the remaining model parameters λ_H and λ_N we evaluate a set of models with $\pm 50\%$ variation in the parameters, see SI: Figure 6-[D] for the comparison of resulting nucleus velocities. Here we observe that even for such strong parameter variations the qualitative behavior of the model remains unchanged underlining the robustness of the calibrated parameter values.

Model for *nop-1; mel-11* RNAi Here we use the parameters of the unperturbed model and enforce the absence of nematic effects by setting $\lambda_N = 0$. Only the active force relaxation is calibrated by fitting the kinetic energy as described in (23). The Myosin state equation parameters are again used as given by (Gross et al., 2019). See SI: Figure 7 for a comparison of experimental data (blue lines) and model results (red lines) for fitted parameters. Again we observe a good reproduction of experimental data for cortex velocities as well as nucleus velocities (effective drag remains unchanged $d = 0.61$), see Figure SI: Figure 7-b.

Nucleus trajectory evaluation From the evaluated nucleus velocities we can evaluate nucleus trajectories by integrating (18) for a given initial nucleus displacement $\mathbf{x}_N(\alpha = 45°)$ for an arbitrary time domain $t \in [0, 1000]$. We describe the obtained nucleus trajectory by $\alpha(t)$. To compare them to experimentally observed trajectories we introduce for a temporal reference point $\hat{t}$. This defined for each set of experimental trajectories (wild type, *nop-1; mel-11* and *ima3*) by choosing $\hat{t}$ such that the average distance to experimental trajectories is minimized. In practice we obtain an average experimental trajectory $\alpha^d(t_i)$ by temporal binning (100 bins) and perform least square error fitting to determine $\hat{t}$

$$\min_{\hat{t}\in\mathbb{R}} \sum_{i=1}^{100} \|\alpha^d(t_i) - \alpha(t_i - \hat{t})\|^2 \to \hat{t}$$

Shape variation To investigate the geometric sensitivity in the mechanical feedback loop we variate the shape of the shape of the ellipsoid. Each shape is characterized along the ratio of long/short body axis a/b. To avoid a change in characteristic length scales we perform such shape variations while preserving volume of the enclosed cytoplasmic bulk. Please note the *ima3* RNAi embryos exhibit an average shape with ellipsoidal axes $[a, b, c] = [21\mu m, 14\mu m, 14\mu m]$. This shape is on the one hand side closer to a sphere compared to the unperturbed control embryos and on the other hand side significantly smaller wrt. volume $V_{IMA}/V_{WT} = 0.57$.

	λ_H	λ_N	λ_A	d	a/b
Unperturbed	10	152.5	11.5	0.61	1.78
nop-1; mel-11	10	0	7	0.61	1.78
ima-3	10	152.5	11.5	0.61	1.48

SI: Table 3: **Model parameter values** [WT] - calibrated parameter set for unperturbed control embryo, [NOP] - calibrated parameter set obtained by calibrating towards cortex velocities observed in *nop-1* and *mel-11* mutants and enforcing $\lambda_N = 0$. Parameters of Myosin state equation $-D_{\mathcal{M}}$, κ_{on}, κ_{off}, $\kappa_{\mathcal{M}}$ are taken from (Gross et al., 2019) while parameter values of nematic free energy τ, λ_D are taken from (Reymann et al., 2016).

2.3 Numerical methods

Given the rotational symmetry of $\mathcal{E}$ along long body axis, the "one way" coupling of cortex and cytoplasmic flows, the instantaneous relaxation of momentum as well as the assumption of a nucleus close to the cortex we apply a catalogue approach for parameter calibration and evaluation of nucleus trajectories.

Assuming a constant nucleus cortex distance $\|\mathbf{x}_N - \Pi_{\mathcal{E}}[\mathbf{x}_N]\| = 3.5$ and nucleus radius $r_N = 3$ we can identify the nucleus position by the polar angle $\alpha = \arctan(x/z) \in [0, \pi/2]$. We discretize this domain equidistant with 30 points. For each α_i we evaluate cortical and cytoplasmic flows as well as nucleus velocities.

All finite element methods are implemented and solved by `AMDiS` toolbox (Vey and Voigt, 2007; Witkowski et al., 2015).

2.3.1 Catalogue evaluation

Geodesic distances: We use a regular triangulation of $\mathcal{E}$ ($10k$ vertices) to formulate a surface FEM (linear Lagrange elements) (Dziuk and Elliott, 2013) and solve the geodesic equations by the heat method of (Crane et al., 2013) with source at $\Pi_{\mathcal{E}}[\mathbf{x}_N(\varphi_i)]$. Thereby we obtain the geodesic distances $d(\mathbf{x})$ on $\mathcal{E}$.

Myosin depletion: The same triangulation and surface FEM approach is used to solve (9) and obtain $\mathcal{M}$ for a depletion centered at $\Pi_{\mathcal{E}}[\mathbf{x}_N(\alpha_i)]$. The non-linearity is handled by a relaxation scheme (100 steps).

Momentum balance and nematic ordering: For the coupled vector valued PDE (14) and Q tensor valued PDE (12) we use a embedded component wise FEM (linear Lagrange elements) (Nestler et al., 2019) on the previous used surface grid, using the penalty specified in (Nestler et al., 2019) with prefactor $\omega_{\mathbf{v}} = \omega_{\mathbf{q}} = 1000$ to ensure tangentiality. Geometric quantities are evaluated from analytical results for $\mathcal{E}$. The coupled system contains nonlinear terms in the active nematic stress. We apply an iterative solution procedure, treating the nonlinear terms explicitly. Details and convergence properties are described in (Reuther and Voigt, 2018; Reuther et al., 2020; Nestler and Voigt, 2022; Brandner et al., 2022).

Cytoplasmic flow: To discretize the volume $\hat{\mathcal{E}}$ we use an adaptive, parametric and regular tetrahedral grid where refinement adaption is used at the interface $\phi \in [0.05, 0.95]$ with $\epsilon = 0.25$. The resulting mesh contains $300k$ vertices. On this mesh we use Taylor-Hood elements to solve the variational formulation of (15). Pressure is fixed by imposing zero mean. Boundary conditions are imposed by using the diffuse domain approach (Li et al., 2009).

2.3.2 Nucleus trajectory

From the catalogue of flow fields for the set of α_i we evaluate the associated nucleus velocities. To evaluate the nucleus trajectory, starting at α_0, we perform explicit time integration and linear interpolation of nucleus velocities from the catalogue.

3 Additional experimental details

3.1 Reduced cortical flows in *nop-1* RNAi embryos

NOP-1 is essential for the formation of a pseudocleavage furrow (Tse et al., 2012). It acts upstream of RHO-1, one of the main regulators of actomyosin in *C. elegans*. We find that 24 hours RNAi of *nop-1* leads to an absence of the pseudocleavage furrow (8 out of 10 embryos), consistent with previous observations (Tse et al., 2012). We also find that cortical flows are reduced (average cortical flow speed: $2.89 \pm 0.65\,\mu m/min$ in *nop-1* RNAi as compared to $4.12 \pm 0.59\,\mu m/min$ in unperturbed control embryos, see SI: Figure 3, SI: Figure 4, SI: Figure 5). To arrive at a condition where cortical flows remain unchanged but the pseudocleavage furrow is absent, we performed double-RNAi of *nop-1* and *mel-11*. MEL-11 is a myosin phosphatase which suppress the activity of myosin in the cortex (Piekny and Mains, 2002). RNAi of *mel-11* is known to increase cortical flow speeds (Piekny and Mains, 2002). Following 24 hours of double RNAi of *nop-1* and *mel-11*, the pseudocleavage furrow is absent (69 out of 69 embryos) and cortical flows are not very different from unperturbed embryos (average cortical flow speed: $3.34 \pm 0.52\,\mu m/min$ in double RNAi of *nop-1* and *mel-11*, as compared to $4.12 \pm 0.59\,\mu m/min$ for unperturbed control embryos, see SI: Figure 3, SI: Figure 4, SI: Figure 5).

3.2 Comparing *ima-3* RNAi embryos and unperturbed embryos

We also sought to evaluate if *ima-3* RNAi, which leads to rounder embryos with smaller aspect ratios, gives rise to additional changes that that might impact on the axis convergence process. Specifically, we measured the cortical flows and myosin concentration on the cortex and in the bulk cytoplasm, in both *ima-3* RNAi and unperturbed embryos. We observed that these values are not significantly different between the *ima-3* RNAi and unperturbed embryos. The myosin concentration in cortex was 79.2 ± 4.3 AU/pixel for *ima-3* RNAi embryos compared to 80.9 ± 13.8 AU/pixel for unperturbed embryos (SI: Figure 11). The myosin concentration in cytosol - 80.3 ± 4.7 AU/pixel for *ima-3* RNAi embryos compared to 76.2 ± 11.1 AU/pixel for unperturbed embryos (SI: Figure 11). We measured average cortical speeds - $3.99 \pm 0.51\,\mu m/min$ for *ima-3* RNAi embryos compared to $4.12 \pm 0.59\,\mu m/min$ for unperturbed embryos (SI: Figure 3, SI: Figure 4, SI: Figure 5). We thus conclude that the axis convergence process in *ima-3* RNAi and unperturbed embryos differ mainly in the smaller aspect ratio and volume (SI: Figure 11) of the *ima-3* RNAi embryos compared to the unperturbed embryos.

4 Contractile ring on ellipsoid: A simple effective model

To provide a physically intuitive understanding of axis convergence, we consider a simpler model of a contractile active ring rotating on an ellipsoid - representing the embryo. As before, we neglect any temporal changes in the shape of the embryo, considering a fixed axisymmetric ellipsoid of axis lengths $a, b, b; a > b$ for the semi-major and semi-minor axes respectively. The long axis (length $2a$) defines the x-axis, while the two short axes (length $2b$ each) define the y- and z- axes, respectively. The contractile ring has only one degree of freedom (it can only rotate about the z-axis). The plane of the contractile ring makes an angle α with the yz plane (see SI: Figure 12b).

Following assumptions are made:

- The ring has a constant line tension T - independent of both the orientation of the ring (i.e. α) and the shape of the ellipsoid (i.e. a, b). In our construction, T has units of force.
- The frictional torque acting on the ring is given by $\gamma \cdot \dot{\alpha}$
- No inertial terms: Torque generated by the ring is perfectly balanced by the torque generated by friction.

Under the above assumptions, we want to calculate $\dot{\alpha}$ as a function of a, b, α for small angles α. Note that a, b are free to vary - we do not assume that our ellipsoid is close to a sphere.

4.1 Motion of contractile ring

We first consider the mechanical energy stored in the contractile ring, which can be given by:

$$E = TC(\alpha) \tag{26}$$

where $C(\alpha)$ is the total circumference of the ring.

We first calculate the circumference of the ring.

4.1.1 Describing the contractile ring

The ring can be described as an intersection of ellipsoid with the plane in which the ring resides. The ring plane makes an angle of α with the y-z plane, and passes through the origin. Thus, it can be described by the equation: $y = -x \cot \alpha$. The ellipsoid itself can be described as $\frac{x^2}{a^2} + \frac{y^2+z^2}{b^2} = 1$. On taking the intersection of the ring plane with the ellipsoid, we get the equation describing the ring:

$$\begin{aligned}
\text{Plane: } & y = -x \cot \alpha \\
\text{Ellipsoid: } & \frac{x^2}{a^2} + \frac{y^2+z^2}{b^2} = 1 \\
\text{Intersection (Ellipse): } & \frac{x^2}{a^2} + \frac{x^2 \cot^2 \alpha + z^2}{b^2} = 1 \implies x^2 \left(\frac{a^2 \cot^2 \alpha + b^2}{a^2 b^2} \right) + \frac{z^2}{b^2} = 1; \quad y = -x \cot \alpha
\end{aligned}$$

Let us define $A = \frac{ab}{\sqrt{a^2 \cot^2 \alpha + b^2}}$. Then, the equation in the intersection part above can be written as: $\frac{x^2}{A^2} + \frac{z^2}{b^2} = 1$ - a form similar to the canonical form for an ellipse. Calling the parametric angle for this ellipse ϕ, we then can write the position vector describing the ring $\vec{r}$ as:

$$\vec{r} = (A \cos \phi, -A \cot \alpha \cos \phi, b \sin \phi)\,; \quad A = \frac{ab}{\sqrt{a^2 \cot^2 \alpha + b^2}}$$

where $\phi \in [-\pi, \pi)$.

Note that the ring is an ellipse in its plane - since the intersection of an ellipsoid and a plane must be an ellipse. This can also be seen by the form by $\|\vec{r}\|^2$:

$$\|\vec{r}\|^2 = A^2 (1 + \cot^2 \alpha^2) \cos^2 \phi + b^2 \sin^2 \phi$$

We can therefore calculate semi-major a_{ring} and semi-minor b_{ring} axes of the ellipse formed by the ring. We directly read them off the expression of $\|\vec{r}\|^2$:

$$\begin{aligned}
a_{ring} &= A\sqrt{1 + \cot^2 \alpha^2} = \frac{ab}{\sqrt{a^2 \cot^2 \alpha + b^2}} \sqrt{1 + \cot^2 \alpha^2} = b\sqrt{\frac{1 + \tan^2 \alpha}{1 + \frac{b^2}{a^2} \tan^2 \alpha}} = \frac{ab}{\sqrt{a^2 \cos^2 \alpha + b^2 \sin^2 \alpha}} \\
b_{ring} &= b \\
e_{ring} &= \sqrt{1 - \left(\frac{b_{ring}}{a_{ring}} \right)^2} = \sqrt{1 - \frac{a^2 \cos^2 \alpha + b^2 \sin^2 \alpha}{a^2}} = \sqrt{\sin^2 \alpha - \frac{b^2}{a^2} \sin^2 \alpha} = \sin \alpha \sqrt{1 - \frac{b^2}{a^2}}
\end{aligned}$$

where e_{ring} is the eccentricity of the ellipse formed by the ring. Note that since the ring rotates near the yz plane (i.e. the plane with the two short axes), the short axis of the ring is just b.

The circumference of the ring is then given by the circumference of this ellipse. The formula for the circumference of an ellipse is:

$$C(\alpha) = 4a_{ring} \int_0^{\frac{\pi}{2}} \sqrt{1 - e_{ring}^2 \sin^2\phi}\, \mathrm{d}\phi \tag{27}$$

4.1.2 Torque generated by contractile ring

Using (26) and (27), we can write down the energy as:

$$E = TC(\alpha) = 4Ta_{ring} \int_0^{\frac{\pi}{2}} \sqrt{1 - e_{ring}^2 \sin^2\phi}\, \mathrm{d}\phi = 4T \frac{ab}{\sqrt{a^2\cos^2\alpha + b^2\sin^2\alpha}} \int_0^{\frac{\pi}{2}} \sqrt{1 - \left(1 - \frac{b^2}{a^2}\right)\sin^2\alpha\sin^2\phi}\, \mathrm{d}\phi$$

The torque can then be expressed as:

$$\begin{aligned}
\tau = -\frac{\mathrm{d}E}{\mathrm{d}\alpha} &= -4T \frac{\mathrm{d}}{\mathrm{d}\alpha}\left(\frac{ab}{\sqrt{a^2\cos^2\alpha + b^2\sin^2\alpha}} \int_0^{\frac{\pi}{2}} \sqrt{1 - \left(1 - \frac{b^2}{a^2}\right)\sin^2\alpha\sin^2\phi}\, \mathrm{d}\phi \right) \\
&= -4T \left[\frac{ab(a^2 - b^2)\cos\alpha\sin\alpha}{\left(a^2\cos^2\alpha + b^2\sin^2\alpha\right)^{3/2}} \int_0^{\frac{\pi}{2}} \sqrt{1 - \left(1 - \frac{b^2}{a^2}\right)\sin^2\alpha\sin^2\phi}\, \mathrm{d}\phi \right. \\
&\quad \left. + \frac{ab}{\sqrt{a^2\cos^2\alpha + b^2\sin^2\alpha}} \int_0^{\frac{\pi}{2}} \frac{-\left(1 - \frac{b^2}{a^2}\right)\sin\alpha\cos\alpha\sin^2\phi}{\sqrt{1 - \left(1 - \frac{b^2}{a^2}\right)\sin^2\alpha\sin^2\phi}}\, \mathrm{d}\phi \right] \\
\implies \tau &= -4T \frac{ab(a^2 - b^2)\sin\alpha\cos\alpha}{\left(a^2\cos^2\alpha + b^2\sin^2\alpha\right)^{3/2}} \int_0^{\frac{\pi}{2}} \frac{\cos^2\phi}{\sqrt{1 - \left(1 - \frac{b^2}{a^2}\right)\sin^2\alpha\sin^2\phi}}\, \mathrm{d}\phi
\end{aligned}$$

Using the Taylor expansion around $\alpha = 0$, we can expand τ to linear order in α as $\tau = \tau|_{\alpha=0} + \frac{\mathrm{d}\tau}{\mathrm{d}\alpha}\big|_{\alpha=0}\alpha + \mathcal{O}(\alpha^2)$. Note that on $\alpha = 0$, the torque also goes to zero. To obtain the linear order expansion, calculate the derivative of the torque at $\alpha = 0$.

$$\begin{aligned}
\left.\frac{\mathrm{d}\tau}{\mathrm{d}\alpha}\right|_{\alpha=0} &= -4T \frac{\mathrm{d}}{\mathrm{d}\alpha}\left[\frac{ab(a^2 - b^2)\sin\alpha\cos\alpha}{\left(a^2\cos^2\alpha + b^2\sin^2\alpha\right)^{3/2}} \int_0^{\frac{\pi}{2}} \frac{\cos^2\phi}{\sqrt{1 - \left(1 - \frac{b^2}{a^2}\right)\sin^2\alpha\sin^2\phi}}\, \mathrm{d}\phi \right]\Bigg|_{\alpha=0} \\
&= -4T \left[\frac{\mathrm{d}}{\mathrm{d}\alpha}\left(\frac{ab(a^2 - b^2)\sin\alpha\cos\alpha}{\left(a^2\cos^2\alpha + b^2\sin^2\alpha\right)^{3/2}} \right)_{\alpha=0} \int_0^{\frac{\pi}{2}} \frac{\cos^2\phi}{\sqrt{1 - \left(1 - \frac{b^2}{a^2}\right)(0)\sin^2\phi}}\, \mathrm{d}\phi \right. \\
&\quad \left. + \frac{ab(a^2 - b^2) * 0 * 1}{\left(a^2(1) + b^2(0)\right)^{3/2}} \frac{\mathrm{d}}{\mathrm{d}\alpha}\left(\int_0^{\frac{\pi}{2}} \frac{\cos^2\phi}{\sqrt{1 - \left(1 - \frac{b^2}{a^2}\right)\sin^2\alpha\sin^2\phi}}\, \mathrm{d}\phi \right)_{\alpha=0} \right] \\
\implies \left.\frac{\mathrm{d}\tau}{\mathrm{d}\alpha}\right|_{\alpha=0} &= -\pi T b \left(1 - \frac{b^2}{a^2}\right)
\end{aligned}$$

Thus, by Taylor expansion, the torque to linear order in α is:

$$\tau \approx \left.\frac{\mathrm{d}\tau}{\mathrm{d}\alpha}\right|_{\alpha=0} \alpha = -\pi T b \left(1 - \frac{b^2}{a^2}\right)\alpha \tag{28}$$

4.1.3 Torque balance

Per our assumption of negligible inertial terms and the form of friction experienced by the ring, the torque balance of the ring can be written as:

$$\tau - \gamma \cdot \dot{\alpha} = 0$$

Putting in the expression for τ we just obtained, we get

$$\dot{\alpha} \approx -\frac{\pi T}{\gamma} b \left[1 - \frac{b^2}{a^2}\right]\alpha \tag{29}$$

4.2 Calculating posteriorization velocity of the male pronucleus v

To get the posteriorization velocity of the male pronucleus v, we assume that the change in the angular position of the male pronucleus from the long axis is the same as the angle α itself. Effectively, the male pronucleus acts as if it is rigidly attached to the normal vector to the ring (SI: Figure 12b). Then, the position of the male pronucleus is given by:

$$\begin{aligned}
\text{On ellipsoid:} \quad & \frac{x_{nucl}^2}{a^2} + \frac{y_{nucl}^2}{b^2} = 1 \\
\text{Angle with x-axis (long axis):} \quad & x_{nucl} = r_{nucl}\cos\alpha, \quad y_{nucl} = r_{nucl}\sin\alpha \\
\implies & \frac{r_{nucl}^2\cos^2\alpha}{a^2} + \frac{r_{nucl}^2\sin^2\alpha}{b^2} = 1 \\
\implies & r_{nucl} = \frac{ab}{\sqrt{a^2\sin^2\alpha + b^2\cos^2\alpha}}
\end{aligned}$$

The posteriorization velocity of the male pronucleus is then given by (for small angles α, velocity is almost parallel to the cortex, hence we can take the full magnitude)

$$v \approx \sqrt{\left(\frac{\mathrm{d}x_{nucl}}{\mathrm{d}t}\right)^2 + \left(\frac{\mathrm{d}y_{nucl}}{\mathrm{d}t}\right)^2} = \sqrt{\dot{r}_{nucl}^2 + r_{nucl}^2\dot{\alpha}^2}$$

For small angle α, $r_{nucl} \approx a - \frac{a^3}{b^2}\alpha^2 + \mathcal{O}(\alpha^3)$ and $\dot{r}_{nucl} = -2\frac{a^3}{b^2}\alpha\dot{\alpha} + \mathcal{O}(\alpha^2)$. Thus,

$$v = \sqrt{\dot{r}_{nucl}^2 + r_{nucl}^2\dot{\alpha}^2} = \dot{\alpha}\sqrt{a^2 - 2\frac{a^4}{b^2}\alpha^2 + 4\frac{a^6}{b^4}\alpha^2 + \mathcal{O}(\alpha^3)} = \dot{\alpha}\left(a + \mathcal{O}(\alpha^2)\right)$$

Therefore, using (29), we get,

$$v \approx -\left[\frac{\pi T}{\gamma}\right]\left[ab\left(1 - \frac{b^2}{a^2}\right)\right]\alpha \tag{30}$$

where we select the negative sign to ensure correspondence with observed behaviour.

4.3 Estimating relation between posteriorization velocity and aspect ratio

To obtain a relation between the posteriorization velocity v and aspect ratio $R = a/b$ for the combined dataset of unperturbed and *ima-3* RNAi embryos, we consider the following procedure:

1. Estimate $\kappa = \left[\frac{\pi T}{\gamma}\right]$ by fitting a straight line to the posteriorization velocity versus angular position graph for the unperturbed embryos (SI: Figure 12c)
2. Use the average semi-minor axis length in the combined dataset to transform (30) into a relation between v and $R = a/b$. (SI: Figure 12d)
3. Compare result from transformed (30) and result from full mathematical model with experimental results. (SI: Figure 12e)

4.3.1 Estimating $\kappa = \left[\frac{\pi T}{\gamma}\right]$

To estimate $\kappa = \left[\frac{\pi T}{\gamma}\right]$, we will use the dataset comprised only of unperturbed embryos. As shown in SI: Figure 12c, we plot the average posteriorization velocity observed in these embryos as a function of the angular position of the male pronucleus, and choose a set of angular positions where the posteriorization velocity looks mostly linear with respect to the angular position. We chose the angular position bins: 3–15 deg.

From the slope $m = -3.37 \times 10^{-3}\,\mu\mathrm{m\,s^{-1}\,deg^{-1}}$ of the linear fit in the selected angular position range (3–15 deg), we can obtain κ using (30) as:

$$m = -\left[\frac{\pi T}{\gamma}\right]\left[a_{un}b_{un}\left(1 - \frac{b_{un}^2}{a_{un}^2}\right)\right] = -\kappa\left[a_{un}b_{un}\left(1 - \frac{b_{un}^2}{a_{un}^2}\right)\right] \implies \kappa = \frac{-m}{a_{un}b_{un}\left(1 - \frac{b_{un}^2}{a_{un}^2}\right)} \tag{31}$$

where the subscript un refers to the semi-major a_{un} and semi-minor b_{un} axes averaged over the unperturbed embryos.

From SI: Figure 11a, we can obtain the values of $a_{un} = 28.7 \pm 1.6\,\mu\mathrm{m}$ and $b_{un} = 16.2 \pm 1.1\,\mu\mathrm{m}$. Using (31), we get the value of κ as:

$$\kappa = \frac{-(-3.37e-3)}{(28.7)(16.2)\left(1 - \frac{(16.2)^2}{(28.7)^2}\right)} = 1.06 \times 10^{-5}\,\mathrm{s^{-1}\,deg^{-1}\,\mu m^{-1}} \tag{32}$$

4.3.2 Transforming (30) into relation between v and $R = a/b$

To then transform (30) into a relation between v and $R = a/b$, we look at the distribution of semi-major a and semi-minor b axes length in the combined dataset (SI: Figure 12d). We note that the the combined dataset has a wide range of a, but b are mostly concentrated around the average value of $15.6 \pm 1.5\,\mu\text{m}$ (see red line in SI: Figure 12d bottom). Therefore, we consider b to be fairly constant throughout the combined dataset, allowing us to rewrite (30) as:

$$v \approx -\left[\frac{\pi T}{\gamma}\right]\left[ab\left(1-\frac{b^2}{a^2}\right)\right]\alpha = [\kappa b^2 \alpha]\left(\frac{a}{b}\left(1-\frac{b^2}{a^2}\right)\right) = C\left(R-\frac{1}{R}\right) \tag{33}$$

where $C = -\kappa b^2 \alpha$ is treated as a constant when considering the relation between v and $R = a/b$ alone. Given the angular positions we choose (3–15 deg), we set $\alpha = 9\,\text{deg}$.

Therefore, C can be calculated as:

$$C = -\kappa b^2 \alpha = (1.06 \times 10^{-5}\,\text{s}^{-1}\,\text{deg}^{-1}\,\mu\text{m}^{-1})(15.6\,\mu\text{m})^2(9\,\text{deg}) = -2.32 \times 10^{-2}\,\mu\text{m/s} \tag{34}$$

4.3.3 Comparing with experimental results and full mathematical model

Comparison between experimental results and the prediction from (33) can be observed in SI: Figure 12e, where the experimental results are black circles with error bars and the prediction from (33) in gray, using the value of C obtained in (34).

To obtain the comparison with the mathematical model (blue curve in SI: Figure 12e), we interpolate the predicted posteriorization velocities in SI: Figure 12a to obtain posteriorization velocity as a function of two variables: angular position and aspect ratio. We follow a procedure similar to the one followed for the experimental results to obtain the prediction from the mathematical model. Using the interpolated predicted posteriorization velocities, we obtain posteriorization velocities for the angular position range 3–15 deg for a given aspect ratio value, and take their average to obtain the prediction for the given aspect ratio. Doing this for the full range of aspect ratios 1.1–2.1 gives us the prediction from the mathematical model (i.e. blue curve in SI: Figure 12e).

5 Supplemental Figures

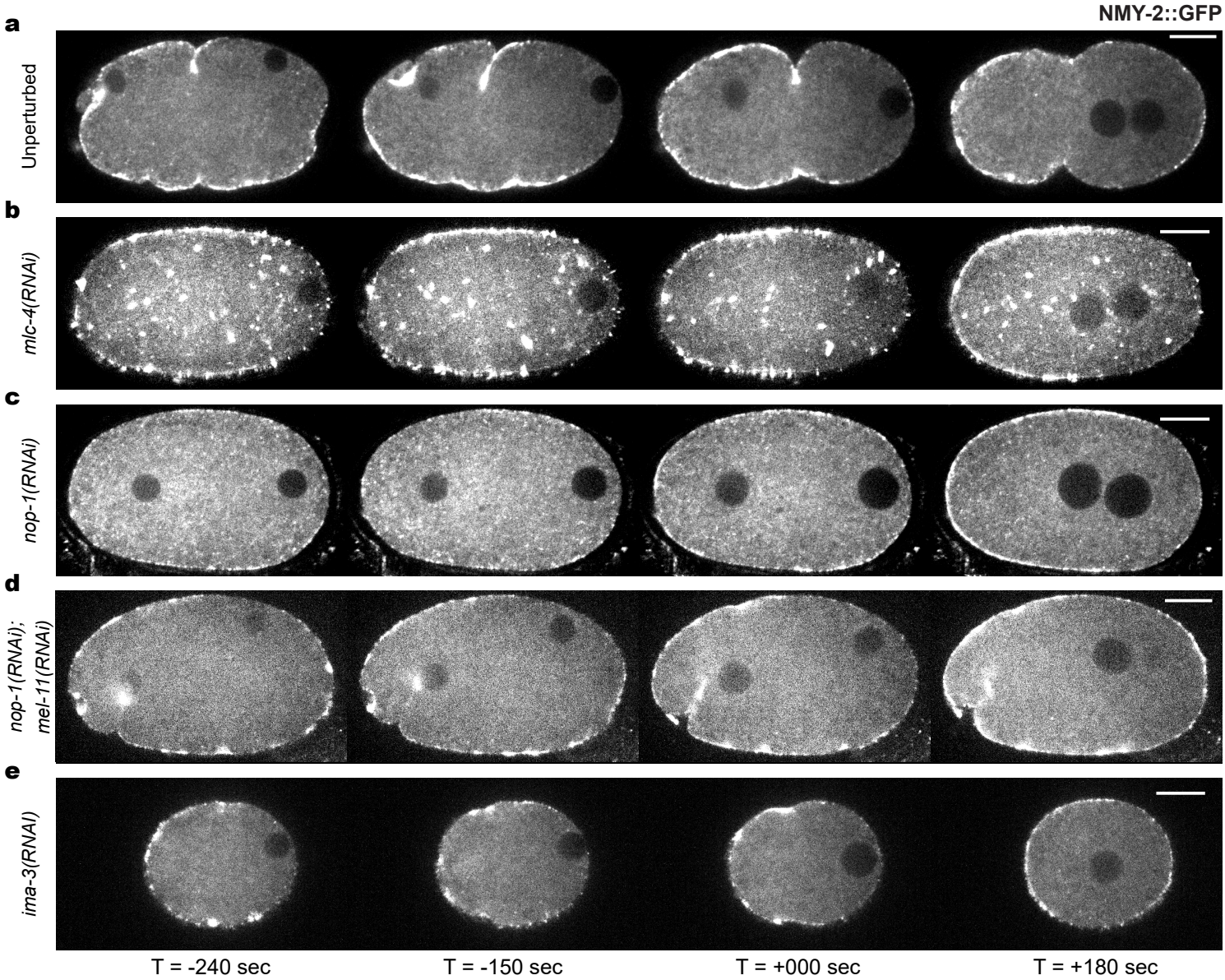

SI: Figure 1: **Comparing axis convergence and posteriorization in different conditions used in this study**
Time lapse images of (a) unperturbed embryos, (b) *mlc-4* RNAi embryos, (c) *nop-1* RNAi embryos,(d) *nop-1; mel-11* RNAi embryos, and (e) *ima3* RNAi embryos labelled with NMY-2::GFP (in gray) during AP axis establishment. t=0 denotes end of posteriorization of the male pronucleus (denoted by green circle). Male pronucleus is identified as the dark circle devoid of myosin on the right (posterior) side of the embryo. Scale bar (for all images): 10 µm.

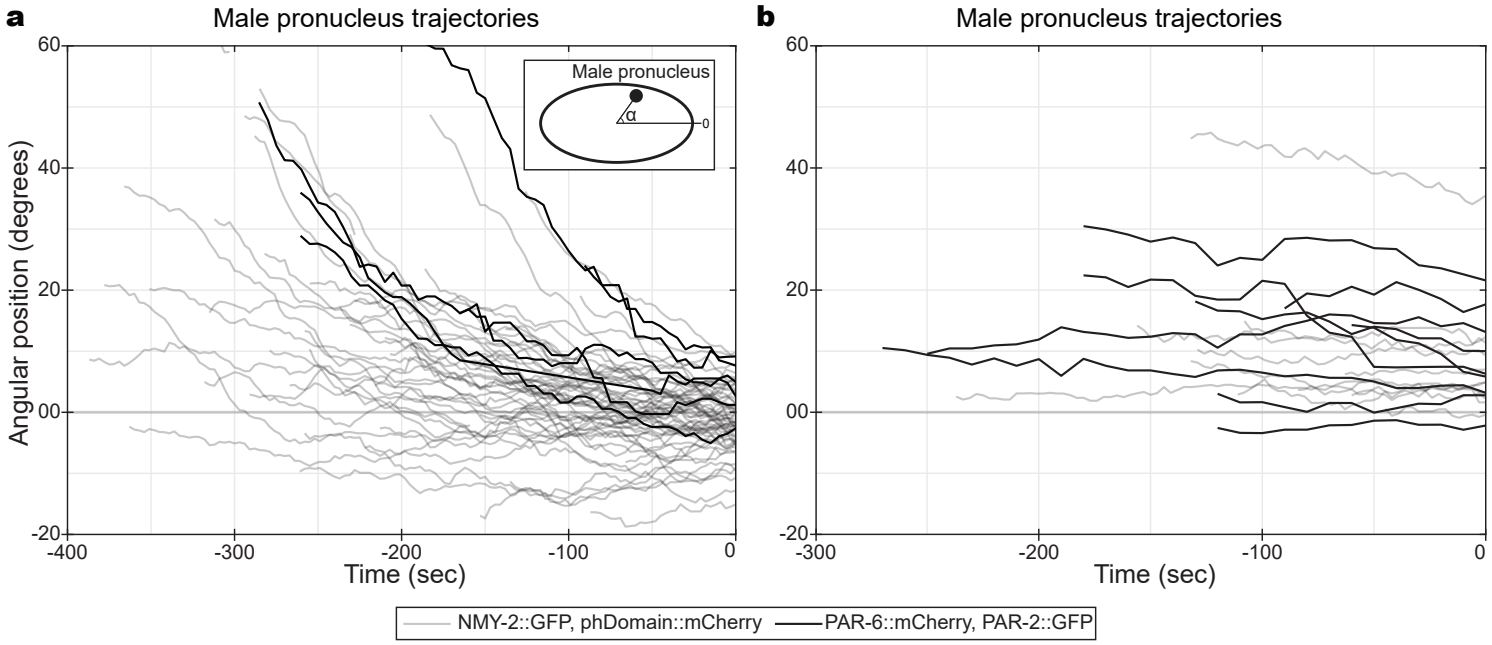

SI: Figure 2: **Comparing male pronucleus posteriorization in SWG070 and TH120**
Angular position of the male pronucleus (on y-axis) as a function of time relative to end of posteriorization (on x-axis), in SWG070 (NMY-2::GFP, phDomain::mCherry labelled, faded black lines) strain and TH120 (PAR-2::GFP, PAR-6::mCherry labelled, dark black lines) strain. Each line represents an individual embryo. a) represents male pronucleus trajectories in unperturbed control embryos, and b) in *mlc-4* RNAi embryos.

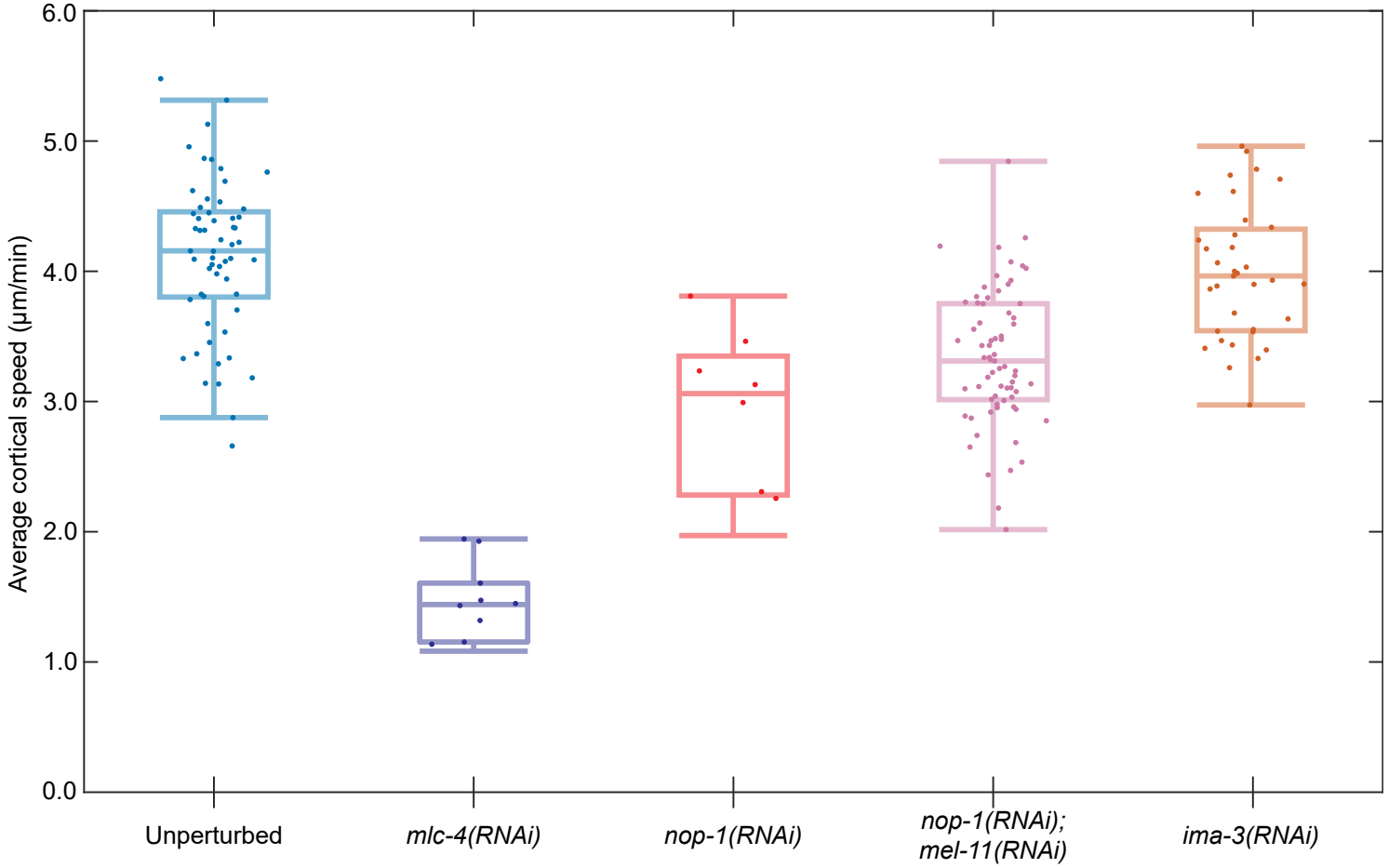

SI: Figure 3: **Comparing cortical flows in different conditions used in this study: Average speed in embryos** Average speed of cortical flows measured in each condition - unperturbed (4.12 ± 0.59 µm/min, blue boxplot and scatter, N = 57), *mlc-4* RNAi (1.45 ± 0.30 µm/min, dark blue boxplot and scatter, N = 10), *nop-1* RNAi (2.89 ± 0.65 µm/min, red boxplot and scatter, N = 8), *nop-1; mel-11* RNAi (3.34 ± 0.52 µm/min, pink boxplot and scatter, N = 69), and *ima-3* RNAi (3.99 ± 0.51 µm/min, orange boxplot and scatter, N = 35).

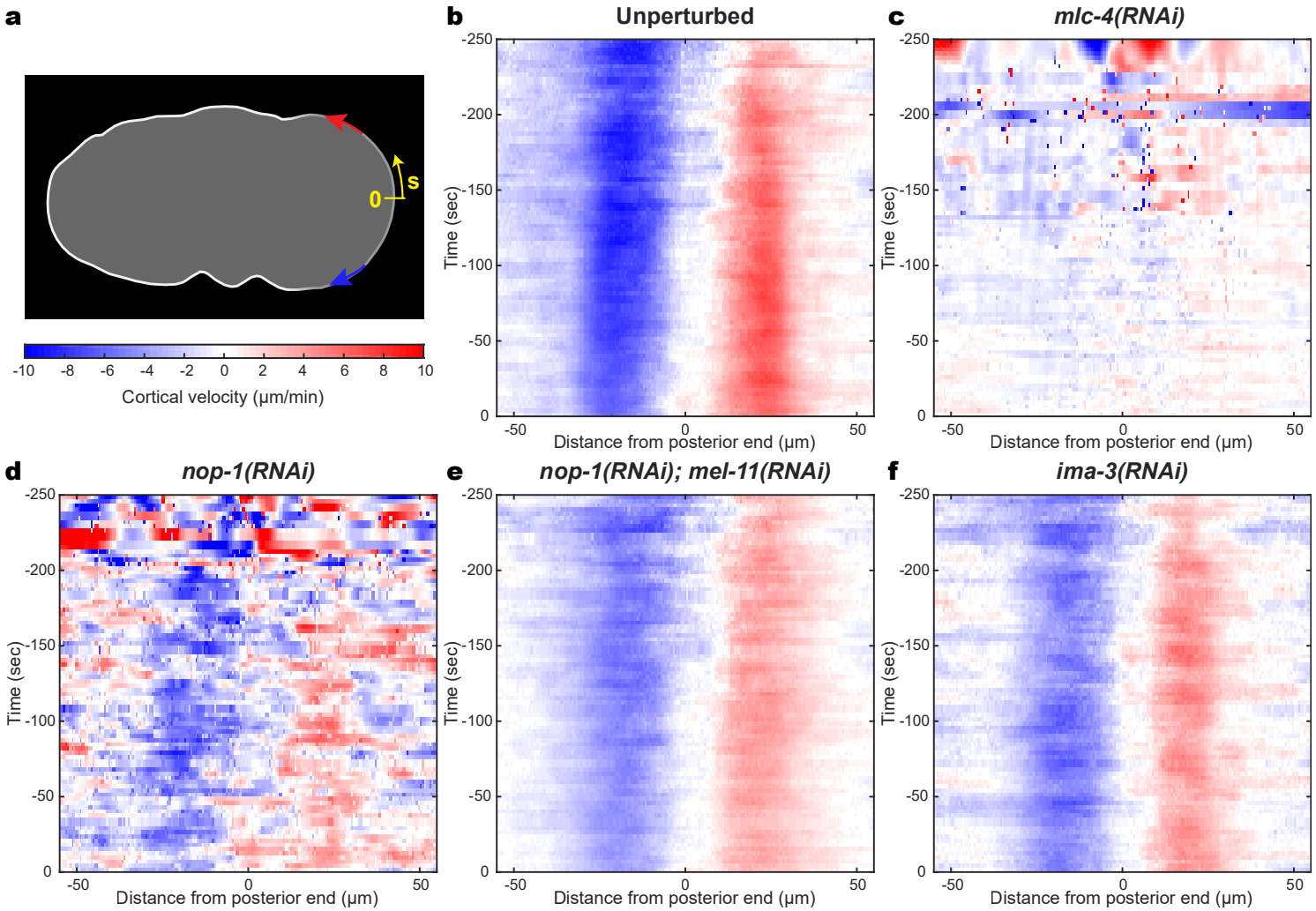

SI: Figure 4: **Comparing cortical flows in different conditions used in this study: Averaged for all angular positions** Flow velocity of the actomyosin cortex as a function of time (along y-axis, in seconds, t=0 denotes end of posteriorization) and position on the cortex (along x-axis, in µm), for different conditions. Cortical flows - whose magnitude is denoted by color - are averaged over all embryos and all angular positions observed for each condition. a) Schematic. s represents the Distance from the posterior end (denoted as 0) along the cortex, with distances in the anti-clockwise direction considered positive. This is represented along the x-axis in all plots. Color bar maps the colors in the plots to cortical velocity in µm/min. Red shades indicates cortical flow pointing in the anti-clockwise direction (i.e. along the increasing direction of s, denoted as positive flow velocity), and blue shades in the clockwise direction (denoted as negative flow velocity). Cortical flows for (b) unperturbed embryos (N = 57), (c) *mlc-4* RNAi embryos (N = 10), (d) *nop-1* RNAi embryos (N = 8), (e) *nop-1; mel-11* RNAi embryos (N = 69), and (f) *ima3* RNAi embryos (N = 35) are plotted.

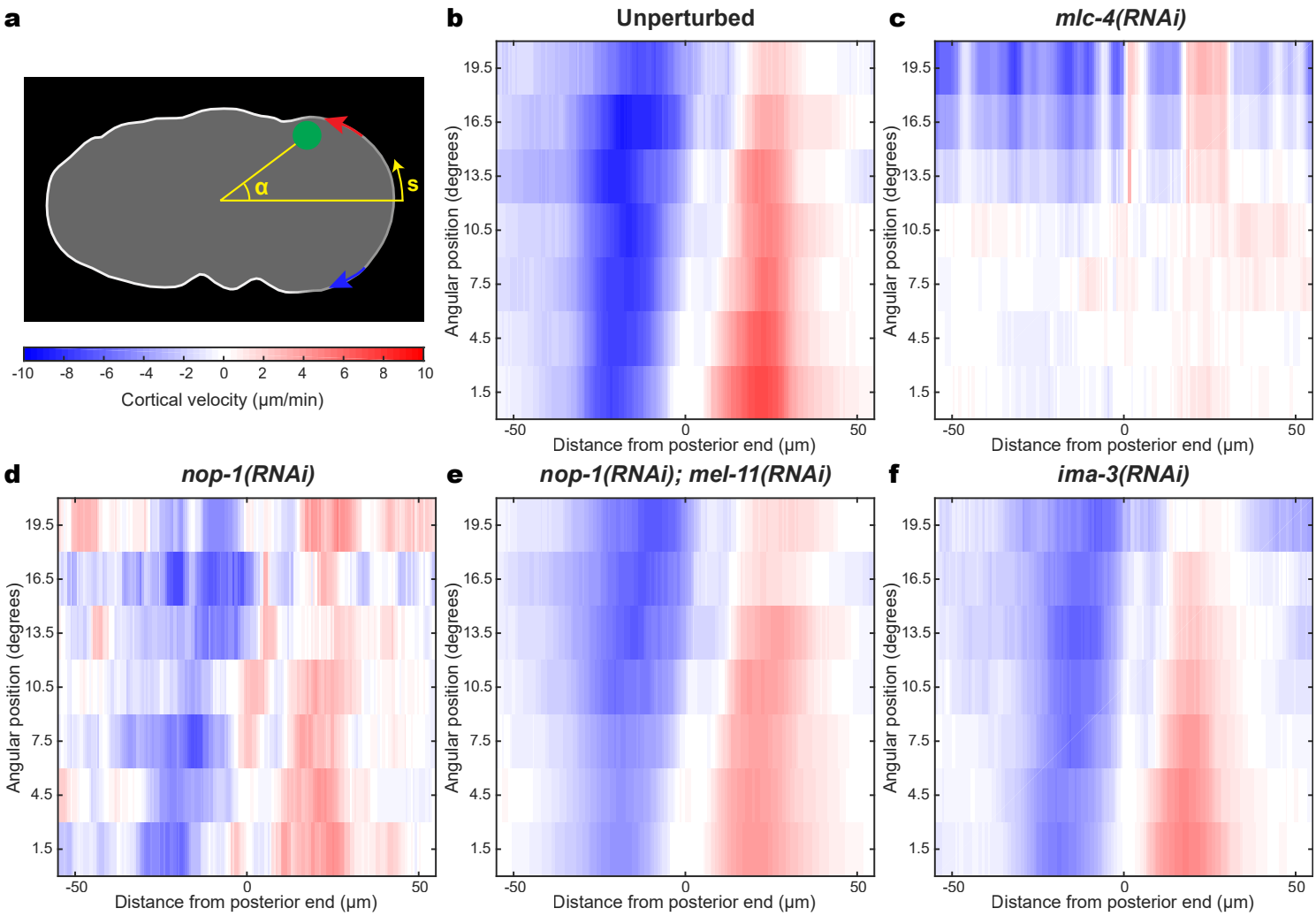

SI: Figure 5: **Comparing cortical flows in different conditions used in this study: Averaged over time**
Flow velocity of the actomyosin cortex as a function of angular position of the male pronucleus (along y-axis, in degrees, t=0 denotes end of posteriorization) and position on the cortex (along x-axis, in μm), for different conditions. Cortical flows - whose magnitude is denoted by color - are averaged over all embryos and all frames for each angular position bin (bins of size 3 deg) observed for each condition. a) Schematic. s represents the Distance from the posterior end (denoted as 0) along the cortex, with distances in the anti-clockwise direction considered positive. This is represented along the x-axis in all plots. α represents the angular position of the male pronucleus. For all embryos in any conditions, cortical flows corresponding to each bin (of size 3 deg) of angular position are averaged. Color bar maps the colors in the plots to cortical velocity in μm/min. Red shades indicates cortical flow pointing in the anti-clockwise direction (i.e. along the increasing direction of s, denoted as positive flow velocity), and blue shades in the clockwise direction (denoted as negative flow velocity). Cortical flows for (b) unperturbed embryos (N = 57), (c) *mlc-4* RNAi embryos (N = 10), (d) *nop-1* RNAi embryos (N = 8), (e) *nop-1; mel-11* RNAi embryos (N = 69), and (f) *ima3* RNAi embryos (N = 35) are plotted.

SI: Figure 6: **Calibration for unperturbed control embryos cortical velocities and model parameter sensitivity:** [A] Cortical velocity profiles (blue: experimental data, red: model) at several nucleus displacement angles $\alpha \in [0°, 19°]$. Profiles are obtained by slice of cortex with plane defined by AP axis and nucleus center. Y-axis denotes flow magnitudes w.r.t. to counter clockwise tangential direction, X-axis denotes (geodesic, signed) distance to $\Pi_{\mathcal{E}}[\mathbf{x}_N]$. [B] Calibration cost landscape for fitting model to data cortical velocity profiles. Green diamond at $\lambda_H = 10,\ \lambda_N = 152.5,\ \lambda_A = 11.5$ indicates best fit. Models without nematic stress $\lambda_N = 0$ fail to recover imbalance of cortical flow fields at higher displacement angles, see [A]. [C] Impact of cortical drag on nucleus velocities in data (x-axis) vs model (y-axis) velocities plot. Modelled cytoplasmic transport velocity $\mathbf{U}_N^1$ (small blue dots), added cytoplasmic transport and cortical drag velocity $\mathbf{U}_N^1 + \mathbf{U}_N^2$ (large blue dots) and nucleus velocities (blue diamonds) with calibrated drag on nucleus $d = 0.61$ recovering observed nucleus velocities. [D] Parameter sensitivities in model. Variation of parameters λ_H and λ_N with nonlinear impact by $\pm 50\%$. Please note, increasing nematic stress relaxation increases nucleus velocities while increasing hydrodynamic length reduces nucleus velocities.

SI: Figure 7: **Calibration for *nop-1; mel-11* cortical velocities:** Cortical velocity profiles (blue: experimental data, red: model) at several nucleus displacement angles $\alpha \in [0°, 19°]$.

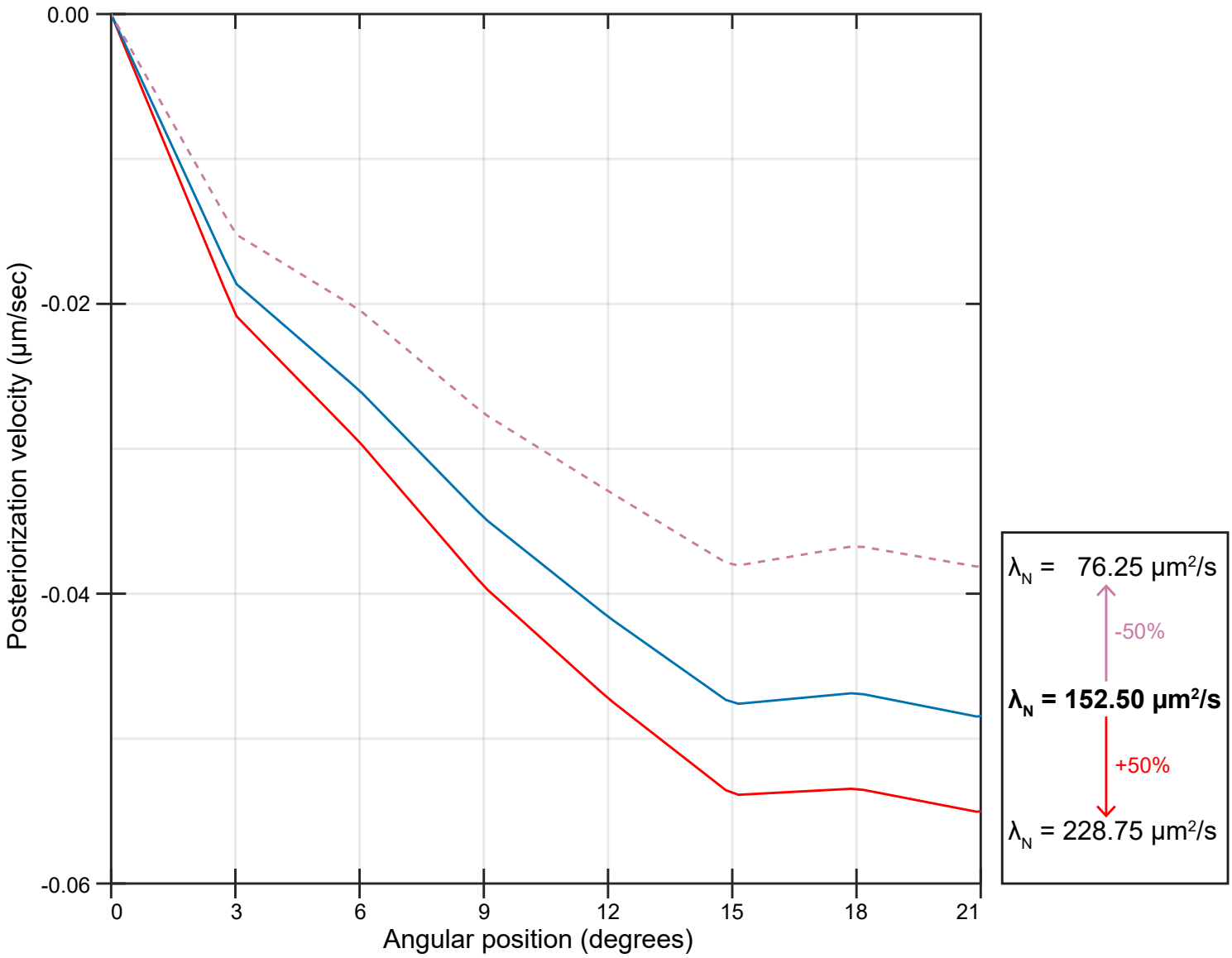

SI: Figure 8: **Modulating λ_N to investigate the role of pseudocleavage furrow-dependent mechanism in axis convergence**

Predicted Posteriorization velocity (y-axis) is plotted as a function of the angular position (x-axis) of the male pronucleus. To investigate the role of pseudocleavage furrow-dependent mechanism, λ_N is modulated. Blue line represents the prediction for the unperturbed embryos (reproduced from SI: Figure 9a), for $\lambda_N = 152.50\,\mu\text{m}^2\,\text{s}^{-1}$. Pink dashed line represents the prediction if λ_N is reduced by 50%, for $\lambda_N = 76.25\,\mu\text{m}^2\,\text{s}^{-1}$ - note the reduced posteriorization speeds. Red line represents the prediction if λ_N is increased by 50%, for $\lambda_N = 228.75\,\mu\text{m}^2\,\text{s}^{-1}$ - note the increased posteriorization speeds.

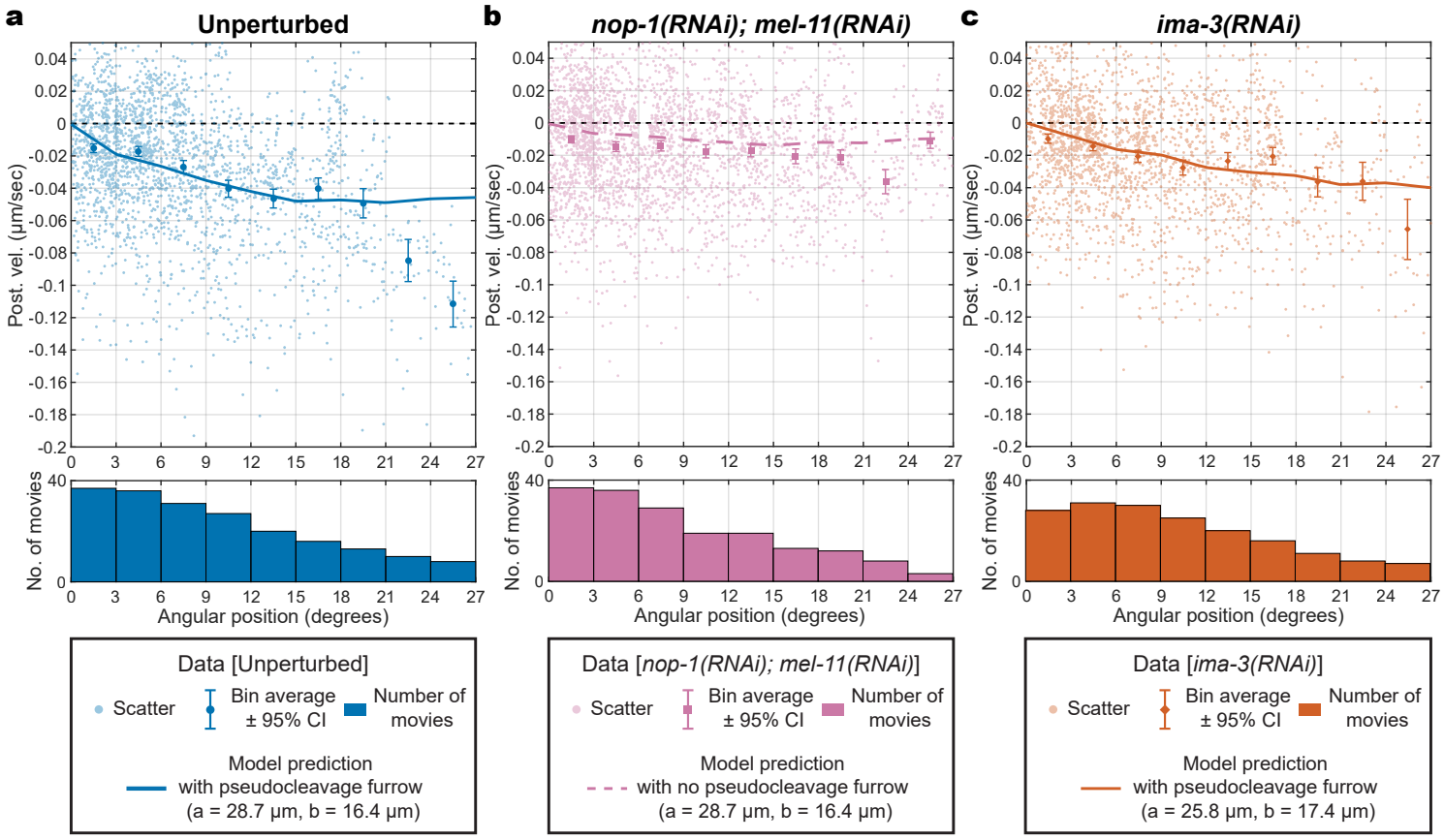

SI: Figure 9: **Posteriorization velocity as a function of angular position for Unperturbed control, *nop-1; mel-11* RNAi and *ima-3* RNAi embryos**

a) Top: Posteriorization velocity of the male pronucleus as a function of its angular position in unperturbed embryos (N = 57), along with full mathematical model prediction. Posteriorization velocity of the male pronucleus (along y-axis, in µm/s) is defined as the velocity component of the male pronucleus along the cell cortex. Angular position of the male pronucleus (along x-axis, in deg) is defined as the angle between the long axis and the line connecting the center of the embryo to the center of the male pronucleus. Blue filled circles with errors bars denote the experimentally measured values in unperturbed embryos, with circles representing average posteriorization velocity and error bars representing the 95% confidence interval in bins of 3 deg each. Smaller light blue circles represent the data scatter - the measured posteriorization velocities for different angular positions. Blue curve denotes the predicted posteriorization velocities using the full mathematical model, including both cytoplasmic flow dependent mechanism and Pseudocleavage furrow dependent mechanisms. Bottom: Histogram of the number of movies (along y-axis) contributing to each angular position (along x-axis) bin. A movie is considered to contribute to an angular position bin if it has any frames with angular positions within that bin. Note that a movie can contribute to multiple bins, as it may contain different frames spanning different angular positions. b) Top: Posteriorization velocity of the male pronucleus as a function of its angular position in *nop-1; mel-11* RNAi embryos (N = 69), along with model prediction considering only the cytoplasmic flow dependent mechanism. See (a) for details. Pink filled squares with errors bars denote the experimentally measured values in unperturbed embryos, with squares representing average posteriorization velocity and error bars representing the 95% confidence interval in bins of 3 deg each. Smaller light pink circles represent the data scatter - the measured posteriorization velocities for different angular positions. Pink dashed curve denotes the predicted posteriorization velocities using the model with only cytoplasmic flow dependent mechanism. Bottom: Histogram of the number of movies (along y-axis) contributing to each angular position (along x-axis) bin. See (a) for details. c) Top: Posteriorization velocity of the male pronucleus as a function of its angular position in *ima-3* RNAi embryos (N = 35), along with model prediction using the full model on embryo with aspect ratio 1.48. See (a) for details. Orange filled diamonds with errors bars denote the experimentally measured values in unperturbed embryos, with diamonds representing average posteriorization velocity and error bars representing the 95% confidence interval in bins of 3 deg each. Smaller light orange circles represent the data scatter - the measured posteriorization velocities for different angular positions. Orange curve denotes the predicted posteriorization velocities using the full model on embryo with aspect ratio 1.48. Bottom: Histogram of the number of movies (along y-axis) contributing to each angular position (along x-axis) bin. See (a) for details.

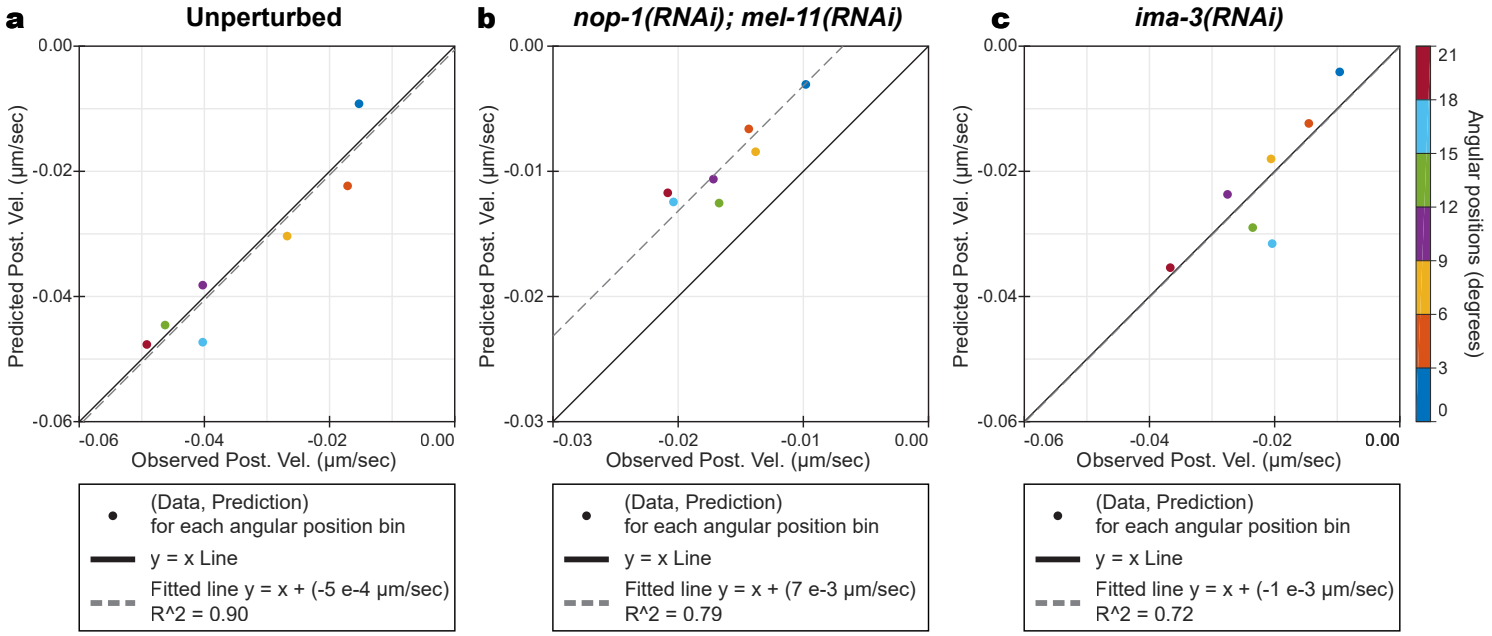

SI: Figure 10: **Evaluating experimental vs model-predicted posteriorization velocities**
Predicted posteriorization velocities (y-axis) using the full mathematical model are plotted against experimentally observed posteriorization velocities (x-axis), for unperturbed embryos (a), *nop-1; mel-11* RNAi embryos (b) and *ima-3* embryos (c). For each case, the corresponding model is used (see SI: Figure 9). Each circle is for an angular bin - represented by color of the circle (see colorbar). Black line represents the $y = x$ line, along which the circles would lie if the prediction was perfect. Grey dashed line represents a fitted line with the same slope as the $y = x$, but with different intercept.

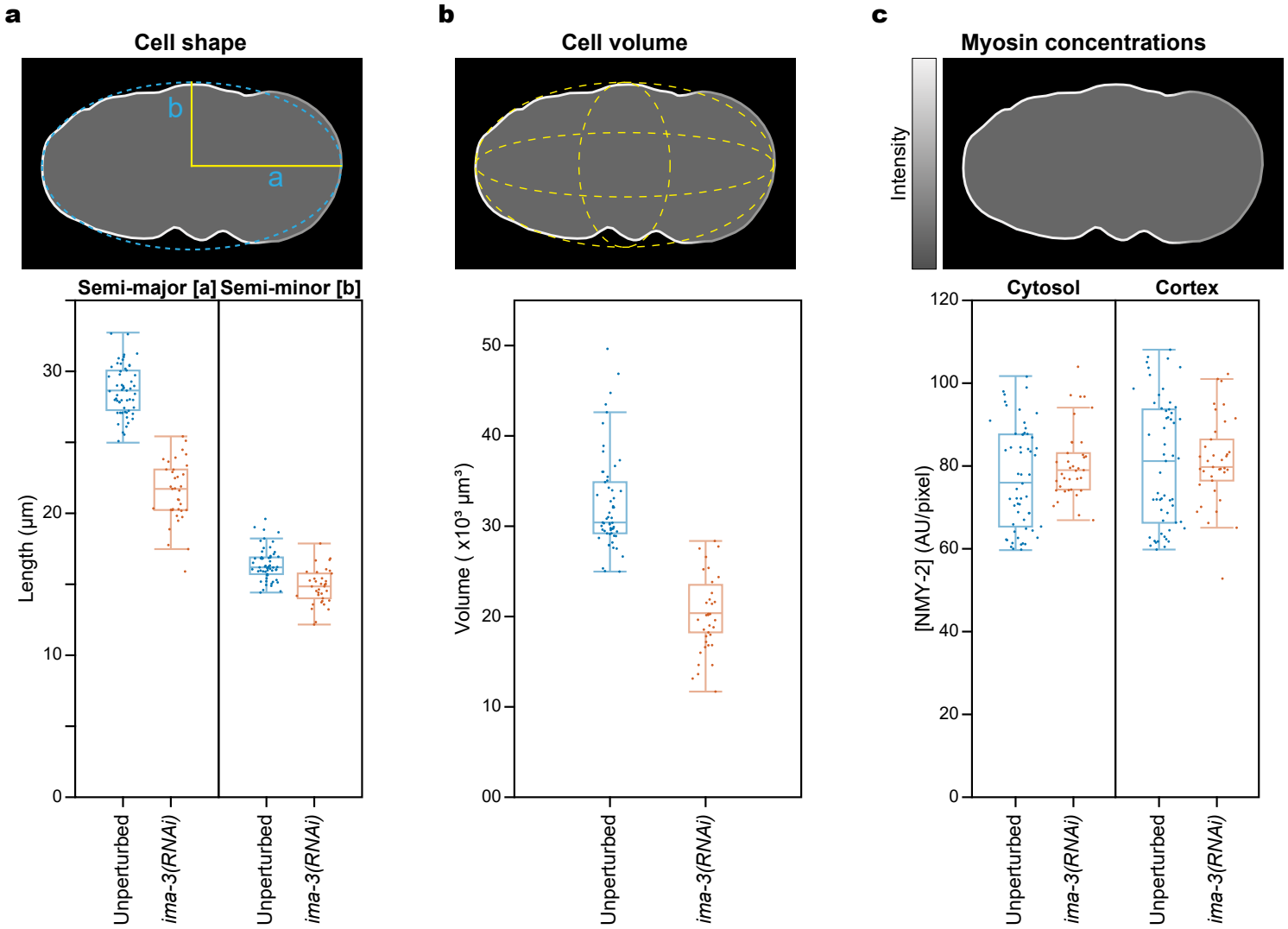

SI: Figure 11: **Comparing unperturbed control embryos and *ima-3* RNAi embryos**
a) Comparing semi-major axis [a] and semi-minor axis [b] lengths between unperturbed and *ima-3* RNAi embryos. Axes lengths are obtained by fitting an ellipse to the cell membrane in the midplane image - schematic represents the definition of a and b. Left: Note the larger difference in semi-major axis length - a $= 28.7 \pm 1.6\,\mu$m in unperturbed (blue boxplot and data scatter) compared to $20.9 \pm 2.2\,\mu$m in *ima-3* RNAi embryos (orange boxplot and data scatter), p-value: 2.02×10^{-18} from two sample t-test. Right: Compare that to the smaller difference in semi-minor axis length - b $= 16.2 \pm 1.1\,\mu$m in unperturbed (blue boxplot and data scatter) compared to $13.8 \pm 0.8\,\mu$m in *ima-3* embryos (orange boxplot and data scatter), p-value: 4.22×10^{-8} from two sample t-test. b) Comparing cell volume between unperturbed and *ima-3* RNAi embryos. For each embryo, we consider an ellipsoid with a semi-major axis (given by the semi-major axis of the ellipse fitted to the cell membrane in the midplane image) and two equal semi-minor axes (given by the semi-minor axis of the ellipse fitted to the cell membrane in the midplane image). Volume of the cell is then estimated as the volume of this ellipsoid. Blue boxplot and data scatter represents unperturbed embryos (Cell volume: $3.26 \pm 0.53 \times 10^4\,\mu m^3$), orange boxplot and data scatter represents *ima-3* RNAi embryos (Cell volume: $2.18 \pm 1.11 \times 10^4\,\mu$m). Note the smaller embryos obtained in *ima-3* RNAi embryos (p-value: 1.59×10^{-6}, two sample t-test). We do not consider the effect of volume changes in the mathematical model. c) Comparing myosin concentration in the cytosol (left) and cortex (right) for unperturbed and *ima-3* RNAi embryos. The cortex is considered as a thin band (of thickness: 15 pixel, inwards) around the cell membrane. Myosin concentration is estimated as the average intensity of NMY2::GFP per pixel in the cortex and cytosol (see schematic on top). In both, Blue boxplot and data scatter represents unperturbed embryos, orange boxplot and data scatter represents *ima-3* RNAi embryos. We observe no significant difference between myosin concentrations in the cortex (80.9 ± 13.8 AU/pixel for unperturbed embryos compared to 79.2 ± 4.3 AU/pixel for *ima-3* RNAi embryos, p-value $=$ 0.72 from two sample t-test) and in the cytosol (76.2 ± 11.1 AU/pixel for unperturbed embryos compared to 80.3 ± 4.7 AU/pixel for *ima-3* RNAi embryos, p-value $= 0.19$ from two sample t-test)

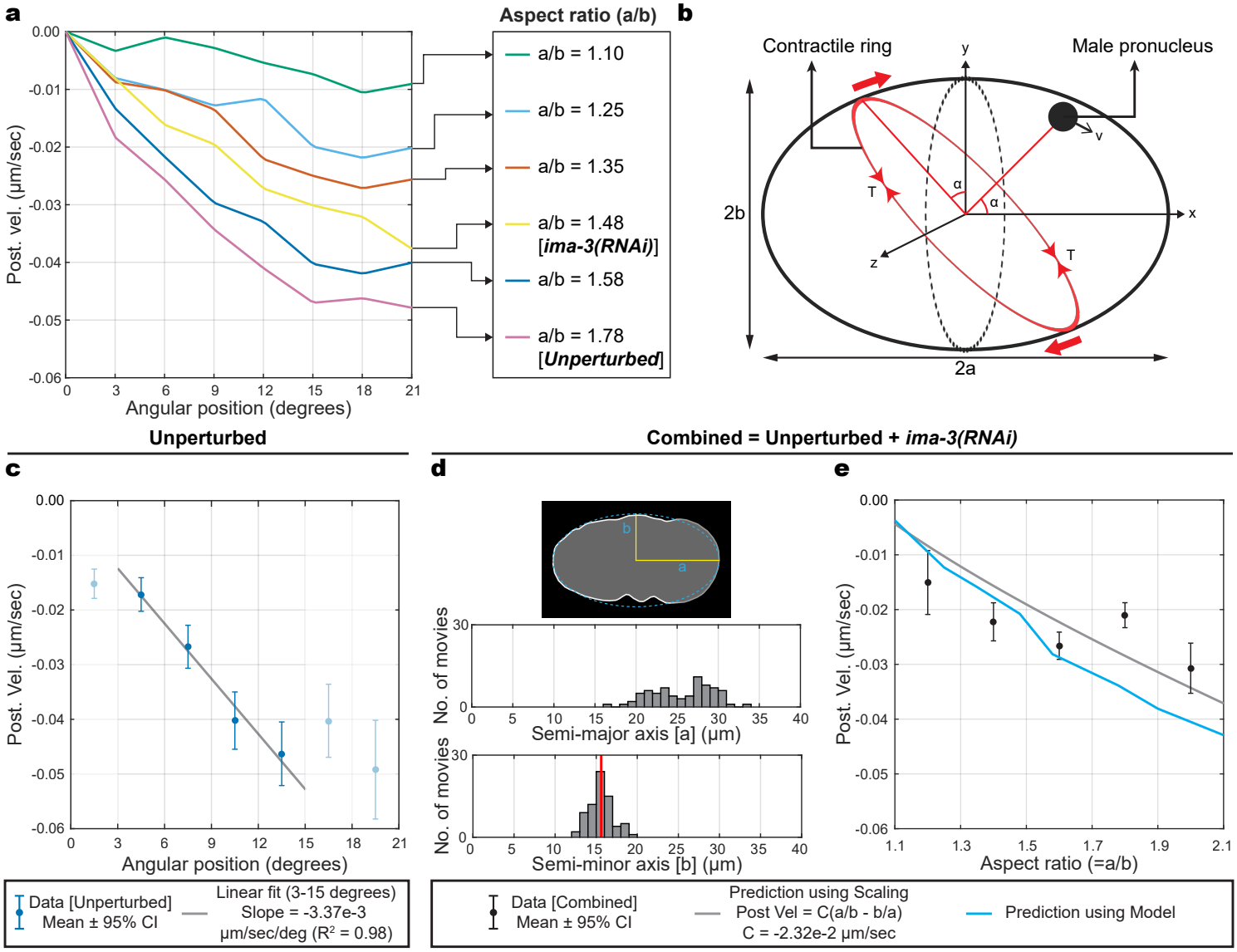

SI: Figure 12: **Exploring influence of embryo geometry on axis convergence using full mathematical model and simple physical model**

a) Predicted posteriorization velocities of the male pronucleus as a function of its angular position, for embryos with different aspect ratios. Embryos with aspect ratios $a/b = 1.25$, 1.35, 1.48, 1.58, 1.78 and 1.90 are considered. Aspect ratio $a/b = 1.48$ is used for predictions on *ima-3* RNAi embryos. Aspect ratio $a/b = 1.79$ is used for predictions on unperturbed embryos. All embryos have the same volume as the unperturbed embryos. Note that posteriorization velocities become larger in magnitude for each angular position bin as the aspect ratio increases, with larger effect observed for higher angles. b) Schematic depicting the effective model of a contractile ring (red ellipse) with fixed line tension (T) moving on an ellipsoid (black thick ellipse) with a long axis of length $2a$ and two short axes of length $2b$. x-axis is along the long axis of the ellipsoid. Both y- and z- axes are along the equal short axes of the ellipsoid (black dashed ellipse resides in the yz plane). The contractile ring is free to rotate about the z-axis (red block arrows), and its position is described by the angle α made between the plane of the contractile ring and the yz-plane. In our effective model, α also describes the angular position of the male pronucleus, considered to always be positioned along the normal to the plane of the contractile ring. (c,d,e) describe the steps used to obtain the scaling parameter using this effective model. c) Fitting a line to posteriorization velocity vs angular position graph for unperturbed embryos - see (a) for details. Blue circles with error bars represent the average posteriorization velocities (with 95% confidence interval) observed in each angular position bin in unperturbed embryos (see SI: Figure 9a). Angular position bins from 3–15 deg are chosen for the linear fit, depicted by grey line. d) Distribution of semi-major a and semi-minor b axis lengths in the combined (unperturbed and *ima-3* RNAi embryos) dataset. Top: Histogram of average semi-major a axis length (along x-axis) for the combined dataset (number of movies on the y-axis). Bins of size 1 µm are used. Note the wide distribution of semi-major axis lengths in the combined dataset. Bottom: Histogram of average semi-minor b axis length (along x-axis) for the combined dataset (number of movies on the y-axis). Bins of size 1 µm are used. Red line denotes the average semi-minor axis length chosen for setting the scaling in posteriorization velocity vs aspect ratio graph. e) Posteriorization velocities (along y-axis) as a function of aspect ratio (along x-axis) of the embryo, averaged for all angular positions in 3–15 deg. Black circles with error bars represent the average posteriorization velocities (with 95% confidence interval) observed in each aspect ratio bin in the combined dataset. Grey line is the prediction obtained using the effective model, and blue line using the full mathematical model.

6 Bibliography

References

Arroyo, M. and DeSimone, A. (2009). Relaxation dynamics of fluid membranes. *Physical Review E*, 79(3):031915.

Bradski, G. (2000). The OpenCV Library. *Dr. Dobb's Journal of Software Tools*.

Brandner, P., Jankuhn, T., Praetorius, S., Reusken, A., and Voigt, A. (2022). Finite element discretization methods for velocity-pressure and stream function formulations of surface Stokes equations. *SIAM J. Sci. Comput.*, 44:A1887–1832.

Brenner, S. (1974). The genetics of caenorhabditis elegans. *Genetics*, 77(1):71–94.

Buades, A., Coll, B., and Morel, J.-M. (2011). Non-local means denoising. *Image Processing On Line*, 1:208–212.

Crane, K., Weischedel, C., and Wardetzky, M. (2013). Geodesics in heat: A new approach to computing distance based on heat flow. *ACM Transactions on Graphics (TOG)*, 32(5):1–11.

De Gennes, P.-G. and Prost, J. (1993). *The physics of liquid crystals*. Number 83. Oxford university press.

Dziuk, G. and Elliott, C. M. (2013). Finite element methods for surface PDEs. *Acta Numerica*, 22:289–396.

Edelstein, A. D., Tsuchida, M. A., Amodaj, N., Pinkard, H., Vale, R. D., and Stuurman, N. (2014). Advanced methods of microscope control using μmanager software. *Journal of Biological Methods*, 1(2).

Geßele, R., Halatek, J., and Frey, E. (2018). Par protein activation-deactivation cycles stabilize long-axis polarization in c. elegans. *bioRxiv*, page 451880.

Gohlke, C. (2019). Read and write tiff files. https://github.com/cgohlke/tifffile.

Gross, P., Kumar, K. V., Goehring, N. W., Bois, J. S., Hoege, C., Jülicher, F., and Grill, S. W. (2019). Guiding self-organized pattern formation in cell polarity establishment. *Nature Physics*, 15(3):293–300.

Harris, C. R., Millman, K. J., van der Walt, S. J., Gommers, R., Virtanen, P., Cournapeau, D., Wieser, E., Taylor, J., Berg, S., Smith, N. J., Kern, R., Picus, M., Hoyer, S., van Kerkwijk, M. H., Brett, M., Haldane, A., del Río, J. F., Wiebe, M., Peterson, P., Gérard-Marchant, P., Sheppard, K., Reddy, T., Weckesser, W., Abbasi, H., Gohlke, C., and Oliphant, T. E. (2020). Array programming with NumPy. *Nature*, 585(7825):357–362.

Hunter, J. D. (2007). Matplotlib: A 2d graphics environment. *Computing in Science & Engineering*, 9(3):90.

Jülicher, F., Grill, S. W., and Salbreux, G. (2018). Hydrodynamic theory of active matter. *Reports on Progress in Physics*, 81(7):076601.

Kamath, R. S. and Ahringer, J. (2003). Genome-wide rnai screening in caenorhabditis elegans. *Methods*, 30(4):313–321.

Li, X., Lowengrub, J., A., R., and Voigt, A. (2009). Solving PDE's in complex geometries: A diffuse domain approach. *Commun. Math. Sci.*, 7:81–107.

Linkert, M., Rueden, C. T., Allan, C., Burel, J.-M., Moore, W., Patterson, A., Loranger, B., Moore, J., Neves, C., MacDonald, D., et al. (2010). Metadata matters: access to image data in the real world. *Journal of Cell Biology*, 189(5):777–782.

MATLAB (2016). *version 9.0.0.341360 (R2016a)*. The MathWorks Inc., Natick, Massachusetts.

McKinney, W. (2010). Data structures for statistical computing in python. In van der Walt, S. and Millman, J., editors, *Proceedings of the 9th Python in Science Conference*, pages 51 – 56.

Middelkoop, T. C., Garcia-Baucells, J., Quintero-Cadena, P., Pimpale, L. G., Yazdi, S., Sternberg, P. W., Gross, P., and Grill, S. W. (2021). Cyk-1/formin activation in cortical rhoa signaling centers promotes organismal left–right symmetry breaking. *Proceedings of the National Academy of Sciences (US)*, 118(20):e2021814118.

Nestler, M., Nitschke, I., Löwen, H., and Voigt, A. (2020). Properties of surface Landau–de Gennes Q-tensor models. *Soft Matter*, 16(16):4032–4042.

Nestler, M., Nitschke, I., and Voigt, A. (2019). A finite element approach for vector-and tensor-valued surface PDEs. *Journal of Computational Physics*, 389:48–61.

Nestler, M. and Voigt, A. (2022). Active nematodynamics on curved surfaces - the influence of geometric forces on motion patterns of topological defects. *Commun. Comput. Phys.*, 31:947–965.

Nitschke, I., Nestler, M., Praetorius, S., Löwen, H., and Voigt, A. (2018). Nematic liquid crystals on curved surfaces: a thin film limit. *Proceedings of the Royal Society A*, 474(2214):20170686.

Nitschke, I., Reuther, S., and Voigt, A. (2020). Liquid crystals on deformable surfaces. *Proc. Roy. Soc. A*, 476:20200313.

Niwayama, R., Shinohara, K., and Kimura, A. (2011). Hydrodynamic property of the cytoplasm is sufficient to mediate cytoplasmic streaming in the caenorhabiditis elegans embryo. *Proceedings of the National Academy of Sciences*, 108(29):11900–11905.

Piekny, A. J. and Mains, P. E. (2002). Rho-binding kinase (let-502) and myosin phosphatase (mel-11) regulate cytokinesis in the early caenorhabditis elegans embryo. *Journal of Cell Science*, 115(11):2271–2282.

Python Core Team (2019). *Python: A dynamic, open source programming language*. Python Software Foundation. Python version 3.8.

Reuther, S., Nitschke, I., and Voigt, A. (2020). A numerical approach for fluid deformable surfaces. *J. Fluid Mech.*, 900:R8.

Reuther, S. and Voigt, A. (2018). Solving the incompressible surface navier-stokes equation by surface finite elements. *Phys. Fluids*, 8:012107.

Reymann, A.-C., Staniscia, F., Erzberger, A., Salbreux, G., and Grill, S. W. (2016). Cortical flow aligns actin filaments to form a furrow. *Elife*, 5:e17807.

Schindelin, J., Arganda-Carreras, I., Frise, E., Kaynig, V., Longair, M., Pietzsch, T., Preibisch, S., Rueden, C., Saalfeld, S., Schmid, B., et al. (2012). Fiji: an open-source platform for biological-image analysis. *Nature Methods*, 9(7):676–682.

Tanaka, H. and Araki, T. (2000). Simulation method of colloidal suspensions with hydrodynamic interactions: Fluid particle dynamics. *Physical Review Letters*, 85(6):1338.

Thielicke, W. and Stamhuis, E. (2014). Pivlab–towards user-friendly, affordable and accurate digital particle image velocimetry in matlab. *Journal of Open Research Software*, 2(1).

Timmons, L., Court, D. L., and Fire, A. (2001). Ingestion of bacterially expressed dsrnas can produce specific and potent genetic interference in caenorhabditis elegans. *Gene*, 263(1-2):103–112.

Tse, Y. C., Werner, M., Longhini, K. M., Labbe, J.-C., Goldstein, B., and Glotzer, M. (2012). Rhoa activation during polarization and cytokinesis of the early caenorhabditis elegans embryo is differentially dependent on nop-1 and cyk-4. *Molecular Biology of the Cell*, 23(20):4020–4031.

Vey, S. and Voigt, A. (2007). AMDiS: adaptive multidimensional simulations. *Computing and Visualization in Science*, 10(1):57–67.

Virtanen, P., Gommers, R., Oliphant, T. E., Haberland, M., Reddy, T., Cournapeau, D., Burovski, E., Peterson, P., Weckesser, W., Bright, J., van der Walt, S. J., Brett, M., Wilson, J., Jarrod Millman, K., Mayorov, N., Nelson, A. R. J., Jones, E., Kern, R., Larson, E., Carey, C., Polat, İ., Feng, Y., Moore, E. W., VanderPlas, J., Laxalde, D., Perktold, J., Cimrman, R., Henriksen, I., Quintero, E. A., Harris, C. R., Archibald, A. M., Ribeiro, A. H., Pedregosa, F., van Mulbregt, P., and Contributors, S. . (2020). SciPy 1.0: Fundamental Algorithms for Scientific Computing in Python. *Nature Methods*.

Witkowski, T., Ling, S., Praetorius, S., and Voigt, A. (2015). Software concepts and numerical algorithms for a scalable adaptive parallel finite element method. *Advances in Computational Mathematics*, 41(6):1145–1177.